Spectroscopic and first principle DFT+ eDMFT study of complex structural, electronic, and vibrational properties of $M_2Mo_3O_8$ (M = Fe, Mn) polar magnets

T. N. Stanislavchuk,[1,*] G. L. Pascut,[2,3] A. P. Litvinchuk,[4] Z. Liu,[5] Sungkyun Choi,[2] M. J. Gutmann,[6] B. Gao,[2] K. Haule,[2] V. Kiryukhin,[2,7] S.-W. Cheong,[7] and A. A. Sirenko[1]

[1]*Department of Physics, New Jersey Institute of Technology, Newark, New Jersey 07102, USA*
[2]*Department of Physics and Astronomy, Rutgers University, Piscataway, New Jersey 08854, USA*
[3]*MANSiD Research Center and Faculty of Forestry, Stefan Cel Mare University (USV), Suceava 720229, Romania*
[4]*Texas Center for Superconductivity and Department of Physics, University of Houston, Houston, Texas 77204, USA*
[5]*Department of Physics, University of Illinois at Chicago, Chicago, Illinois 60607-7059, USA*
[6]*ISIS Facility, STFC-Rutherford Appleton Laboratory, Didcot OX11 OQX, United Kingdom*
[7]*Rutgers Center for Emergent Materials and Department of Physics and Astronomy, Rutgers University, Piscataway, New Jersey 08854, USA*

(Received 1 August 2019; revised 18 July 2020; accepted 25 August 2020; published 17 September 2020)

Optical spectroscopy, x-ray diffraction measurements, density functional theory (DFT), density functional theory + embedded dynamical mean-field theory (DFT+ eDMFT), and crystal-field calculations have been used to characterize structural and electronic properties of hexagonal $M_2Mo_3O_8$ (M = Fe, Mn) polar magnets. Our experimental data are consistent with the room-temperature structure belonging to the space group $P6_3mc$ for both compounds. The experimental structural and electronic properties at room temperature are well reproduced within DFT+ eDMFT method, thus establishing its predictive power in the paramagnetic phase. With decreasing temperature, both compounds undergo a magnetic phase transition, and we argue that this transition is concurrent with a structural phase transition (symmetry change from $P6_3mc$ to $P6_3$) in the Fe compound and an isostructural transition (no symmetry change from $P6_3mc$) in the Mn compound.

DOI: 10.1103/PhysRevB.102.115139

I. INTRODUCTION

Materials with coupled magnetic and electric degrees of freedom have attracted significant attention due to their importance in designing novel electronic devices, such as magnetoelectric (ME) tunneling junctions, weak magnetic field sensors, microwave phase shifters, low-energy consuming electronics, and many other applications [1–4]. For a ME effect to be observed, the time-reversal and space-inversion symmetries should be broken. This is always fulfilled in multiferroics, i.e., materials with simultaneous magnetic and electric orders, which stimulated a growing interest in their properties. Many multiferroics are multidomain compounds which weakens the total ME effect averaged among all domains. Special poling procedures are required to achieve their full ME potential. In contrast, polar magnets, which are a subclass of type-I multiferroics [5] and characterized by crystallization in a polar structure and development of magnetic order at lower temperatures, can often be grown as monodomain, which is beneficial for ME applications. In this paper, using experimental and theoretical techniques, we study the representative compounds of the $M_2Mo_3O_8$ (M is a transition metal) polar magnet family [6,7], which possess strong spin-lattice coupling resulting in rich ME properties. In particular, a large tunable ME effect was reported for $M_2Mo_3O_8$ polar magnets in both static [8–10] and dynamic regimes [11–13]. Also, a giant thermal Hall effect has recently been observed in $Zn_xFe_{1-x}Mo_3O_8$ crystals, revealing the influence of spin-lattice coupling on low-energy acoustic phonon modes [14].

ME properties of the system can be described with a ME tensor, the symmetry of which is determined by crystallographic and magnetic symmetries. We have found that the crystal structure of the $M_2Mo_3O_8$ at room temperature belongs to a polar $P6_3mc$ space group and consists of M^{2+} and Mo^{4+} layers stacked along the c axis [see Fig. 1(a)]. The M^{2+} layer is composed of the corner-sharing MO_6 octahedra and MO_4 tetrahedra. The orientation of the vertices of the latter determines the direction of electric polarization along the c axis. Magnetic M^{2+} layers are separated by nonmagnetic trimerized MoO_6 octahedra [see Fig. 1(b)]. Both compounds, $Mn_2Mo_3O_8$ and $Fe_2Mo_3O_8$, order magnetically below T_C = 41 K for the Mn and T_N = 60 K for the Fe compound with the magnetic moments collinear with the c axis [15]. Neutron scattering experiments showed that the magnetic structures are of antiferromagnetic and ferrimagnetic types for the Fe and Mn compounds, respectively, with different magnetic moments on the octahedral and tetrahedral sites [see Fig. 1(c)] [15]. Within each M^{2+} layer, the magnetic moments on the octahedral and tetrahedral sites are aligned antiferromagnetically, thus giving rise to a net ferromagnetic intralayer moment [see Fig. 1(c)]. For the Mn compound, the ferromagnetic intralayer moments are coupled ferromagnetically, resulting in the ferrimagnetic (FRM) order type. In

*Author to whom correspondence should be addressed: stantar@njit.edu

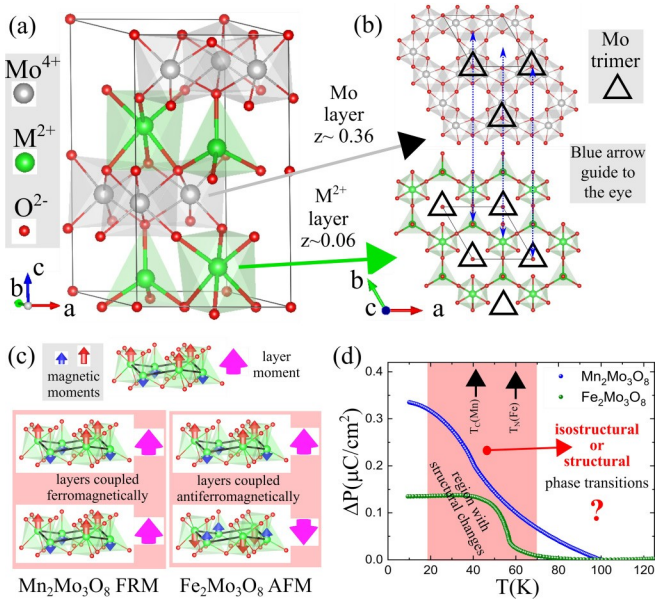

FIG. 1. Schematic overview of the crystal, magnetic, and electric properties. (a) Room-temperature crystal structure for $M_2Mo_3O_8$; (b) layer arrangements of the MoO_6, MO_6, and MO_4 polyhedra; (c) schematic representation of the magnetic properties; and (d) temperature dependence for the variation of the electric polarization for $M_2Mo_3O_8$ (M = Fe, Mn) along the c axis (the data were reproduced from Ref. [10]). The shaded area suggesting the region with structural changes in (d) is only a guide for the eye.

contrast, for the Fe compound, these intralayer moments are coupled antiferromagnetically, thus hiding the ferromagnetic intralayer moment and giving rise to antiferromagnetic (AFM) order type [see Fig. 1(c)]. Recently it was shown that the ferromagnetic intralayer moment can be revealed in the Fe compound either by application of a magnetic field $H \parallel c$ or by Zn doping, thus enabling switching between AFM and FRM order types, which has a substantial implication to the large magnetic-field-tunable ME effect reported in the Fe compound [8,9,16].

Combined studies of specific heat, pyroelectric current, and dielectric susceptibility suggested that ordering of M spins is concurrent with structural changes in both Fe and Mn compounds, see Fig. 1(d) and Refs. [8,10]. Also, it has been shown that the changes in polarization $P(T)$ are similar in both Mn and Fe compounds [see Fig. 1(d)] [10], which implies that the atomic displacements are of the same order of magnitude. The changes in polarization for the Fe compound have been reproduced using a simple model based on the difference between the atomic coordinates in the ordered state (obtained by DFT + U) and in the paramagnetic state (determined by experiment) [8]. Although these calculations could reproduce the order of magnitude for $P(T)$ and suggest that the origin of these structural changes are the exchange striction effects, no information about the low temperature (LT) symmetry of these materials was obtained [8]. Thus, an open question still exists about the type of the structural phase transition.

The goals of this work are (I) to unravel the nature of these atomic displacements occurring through the magnetic transition and learn if they are consistent with breaking the high temperature (HT) symmetry (structural phase transition) or with preserving it (isostructural phase transition), and (II) to prove the predictive powers of the eDMFT method for the structural and electronic properties in the paramagnetic state.

To answer these questions, we revised the room-temperature crystal structures using single-crystal x-ray diffraction, performed infrared (IR) and Raman studies of phonon modes in the temperature range 300–5 K, and investigated the electronic properties, such as the band gap magnitude and the crystal-field levels in $M_2Mo_3O_8$ (M = Fe, Mn) compounds. The reason we chose spectroscopic techniques to probe the symmetry changes across the magnetic transitions is because the number of spectroscopically accessible electronic and lattice excitations is determined by the crystal's symmetry, and thus these techniques are very sensitive to phase transitions upon which the symmetry changes. To the best of our knowledge, only unpolarized IR transmission and Raman measurements on polycrystalline $M_2Mo_3O_8$ (M = Co) samples have been reported in the literature so far [17]. We have employed density functional theory (DFT) and density functional theory + embedded dynamical mean-field theory (DFT+ eDMFT) to understand better the interplay of the structural and electronic degrees of freedom in the paramagnetic state of these materials with complex crystal structures, see Fig. 1. In addition, we have performed crystal-field calculations of electronic states of Fe^{2+} ions both in tetrahedral and octahedral environments to separate electronic and lattice contributions to the far-infrared and Raman spectra of $Fe_2Mo_3O_8$ in the magnetically-ordered state.

Based on our experimental and theoretical approaches we will show that (I) the magnetic transition is concurrent with a structural phase transition in the Fe compound (from $P6_3mc$ to $P6_3$) and an isostructural phase transition in the Mn compound; (II) there is an overall good agreement between the DFT calculated and room-temperature experimental infrared and Raman phonon modes apart from some low-frequency modes positioned below 200 cm^{-1} in the Fe compound; (III) the electronic and structural properties at finite temperature (in the paramagnetic state) reproduced by DFT + eDMFT are in very good agreement with the experiment, thus confirming the predictive powers of the DFT + eDMFT method at finite temperature; and (IV) the group of spectral lines observed in the IR and Raman spectra of $Fe_2Mo_3O_8$ in 3400–3500 cm^{-1} range corresponds to electronic $d - d$ transitions in tetrahedrally coordinated Fe^{2+} ions and is well reproduced by the crystal-field calculations.

II. SAMPLES, EXPERIMENTAL TECHNIQUES, AND CALCULATIONS

$M_2Mo_3O_8$ (M = Fe, Mn) and $FeZnMo_3O_8$ were grown using a chemical vapor transport method at the Rutgers Center for Emergent Materials [8]. Single crystals with naturally terminated faces had a typical size of 0.5 × 0.5 × 0.5 mm^3. Different samples with crystal faces that contained two different orientations of the c axis, namely in the plane of the sample and perpendicular to it, have been selected for spectroscopic experiments. Far-infrared (FIR) reflectivity measurements were performed for the electric field of light

directed along and perpendicular to the *c* axis of the crystals in the 60– 7000 cm^{-1} spectral range using a Bruker v80 interferometer with a glowbar light source and a 15× Schwarzschild objective. The spectral resolution in the far-IR experiments was 2 cm^{-1}. Micro-Raman experiments have been performed for the laser light excitation and collection along and perpendicular to the *c* axis of the crystals in the backscattering configuration using a 532 nm laser, a LN_2-cooled CCD detector, and a single-grating Princeton Instruments SpectraPro SP-2556 Imaging Spectrograph, which provided a spectral resolution of about 2 cm^{-1}. For both FIR reflectivity and Raman measurements, samples were placed in a LHe-flow optical cryostat, which allowed us to perform measurements at temperatures down to 5 K. Ellipsometric measurements were performed at room temperature only in the near-IR to ultraviolet (UV) spectral range at 65° angle of incidence using a J. A. Woollam M-2000 spectroscopic ellipsometer at the Center for Functional Nanomaterials at Brookhaven National Lab (CFN-BNL).

Single crystal diffraction data were collected on a Rigaku Oxford Diffraction SuperNova diffractometer equipped with an Atlas CCD-detector and Cu$K\alpha$ radiation at $T = 300$ K. Data collection, cell refinement, and data reduction were carried out using CRYSALISPRO [18]. The JANA2006 software [19] was used for structure refinement. The absorption correction was done analytically using a multifaceted crystal model [20]. Extinction corrections were performed using an isotropic Becker & Coppens, type 1, GAUSSIAN [21]. Figures of structures were generated using VESTA [22]. Figures were prepared in INKSCAPE [23].

Lattice dynamics properties of $Fe_2Mo_3O_8$ and $Mn_2Mo_3O_8$ crystals were calculated within the density functional theory using the *ab initio* norm-conserving pseudopotential method as implemented in the CASTEP package [24]. Equilibrium atomic structures were obtained from the total-energy minimization method within DFT. Electron exchange and correlation interactions have been modeled within the local density approximation [24,25]. Plane wave basis set cutoff was 750 eV that allowed energy convergence within 10^{-7} eV. The lattice was optimized until residual forces on atoms in their equilibrium positions did not exceed 5 meV/Å. Lattice dynamic properties of both compounds were further assessed via a finite displacement method on a 2× 2 × 1 supercell [26]. Integration over the Brillouin zone was performed over the 5 × 5 × 2 Monkhorst-Pack grid in reciprocal space [27]. For both materials, no imaginary modes were predicted by the theory.

For calculating electronic properties and optimizations of internal coordinates, we used both (I) the density functional theory as implemented in WIEN2K package [28] and (II) a fully charge-self-consistent dynamical mean-field theory method, as implemented in Rutgers DFT + eDMFT code [29–31]. Throughout the rest of the paper we will refer to DFT+ eDMFT method as eDMFT. For the DFT part, we used the generalized gradient approximation Perdew-Burke-Ernzerhof (GGA-PBE) functional [32], RKmax = 7·0, and 312 *k*-points in the irreducible part of the first Brillouin zone. For optimizations of internal coordinates [33,34], a force criterion of 10^{-4} Ry/bohr was adopted. In order to solve the auxiliary quantum impurity problem, a continuous-time quantum Monte Carlo method in the hybridization-expansion limit (CT-HYB) was used [35], where the five *d* orbitals for the Mn and Fe ions (grouped according to the local point group symmetry) were chosen as our correlated subspaces in a single-site eDMFT approximation. For the CT-HYB calculations, up to 400 million Monte Carlo steps were employed for each Monte Carlo run. In all runs, the temperature was set to 500 K, i.e., slightly higher than room temperature, to obtain faster convergence of the calculations for these materials with the complex crystal structure.

To define the eDMFT projector, we used the quasielectronic orbitals by projecting bands in the large hybridization window (− 10 to + 10 eV with respect to the Fermi level), in which partially screened Coulomb interaction has values of $U = 10$ eV and $J_H = 1$ eV in both Mn and Fe ions. A nominal double counting scheme was used [36], with the *d* -orbital occupations for double counting corrections for Mn and Fe chosen to be 5 and 6, respectively.

To explain $d - d$ electronic transitions in Fe^{2+} ions in the magnetically ordered state of $Fe_2Mo_3O_8$, we have used a phenomenological crystal-field theory in the formalism of Stevens operators [37,38].

III. EXPERIMENTAL AND THEORETICAL RESULTS

A. HT structural properties

The room-temperature crystal structures of $Mn_2Mo_3O_8$ and $Fe_2Mo_3O_8$ compounds have been revised using single-crystal x-ray diffraction. Our findings at room temperature are consistent with the previously reported space group symmetry and structural parameters [6,7,39–41]. The good quality of our refinements can be seen from the plot of the observed vs calculated structure factors squared, $|F|^2$, satisfying $|F|^2 > 3\sigma(|F|^2)$ shown in Figs. 2(a) and 2(b). From the total number (5140/4325 for $Mn_2Mo_3O_8$/$Fe_2Mo_3O_8$) of measured reflections, we obtained 271 /271 unique reflections satisfying $|F|^2 > 3\sigma(|F|^2)$ for $Mn_2Mo_3O_8$/$Fe_2Mo_3O_8$ compounds that are contributing to the least-squares refinements calculation (reflections related by symmetries are merged together). The ratio data/parameters used in the "full least-squares on F^2" refinement method was 271/32 for each compound. Other parameters commonly used to characterize the data refinements are shown as insets in Figs. 2(a) and 2(b). These parameters are defined as follows: (I) the residual factor R_1 for the reflections used in the refinements, $R_1 = \frac{|F_{obs} - F_{calc}|}{|F_{obs}|}$; (II) the weighted residual factor wR_2 for the reflections used in the refinements, $wR_2 = \sqrt{\frac{w(F^2_{obs} - F^2_{calc})^2}{(F^2_{obs})^2}}$, where $w = \frac{1}{[\sigma(F^2_{obs})]^2 + 0.0004F^4_{obs}}$; and (III) the goodness of fit $S = \sqrt{\frac{w(F^2_{obs} - F^2_{calc})^2}{N_{ref} - N_{param}}}$. In these equations, F_{obs} and F_{calc} represent the observed and calculated structure factors, N_{param} represents the number of refined parameters, N_{ref} represents the number of unique reflections used in the refinement, and the sum is taken over all N_{ref} reflections.

Our crystals reveal the high quality by showing that more than 98% of detected reflections are indexed by a single hexagonal domain corresponding to the $P6_3mc$ hexagonal

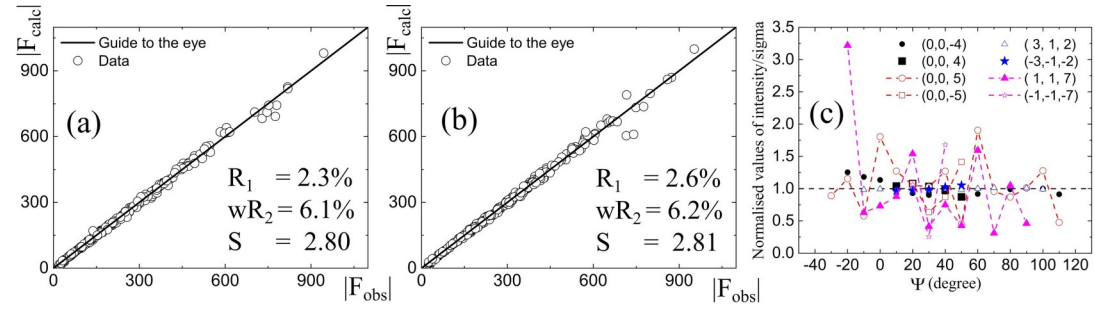

(d) **$Mn_2Mo_3O_8$** SPG: $P6_3mc$ No. 186

a = b = 5.7975(2) Å c = 10.2707(5) Å α = β = 90° γ = 120°

Site		X	Y	Z	U
Mn1	2b	1/3	2/3	0.0659(2)	0.0096(7)
Mn2	2b	1/3	2/3	0.6277(4)	0.0074(7)
Mo	6c	0.14591(11)	0.85409(5)	0.36469(9)	0.0067(3)
O1	2a	0	0	0.0000(11)	0.013(3)
O2	2b	1/3	2/3	0.2649(13)	0.009(3)
O3	6c	0.4878(7)	0.5122(7)	0.4719(7)	0.0035(19)
O4	6c	0.8356(7)	0.1644(7)	0.2492(9)	0.010(2)

(e) **$Fe_2Mo_3O_8$** SPG: $P6_3mc$ No. 186

a = b = 5.7753(4) Å c = 10.0588(5) Å α = β = 90° γ = 120°

Site		X	Y	Z	U
Fe1	2b	1/3	2/3	0.0623(2)	0.0096(7)
Fe2	2b	1/3	2/3	0.6226(4)	0.0083(7)
Mo	6c	0.14605(12)	0.85394(6)	0.36031(10)	0.0067(3)
O1	2a	0	0	0.0000(10)	0.008(3)
O2	2b	1/3	2/3	0.2584(11)	0.007(3)
O3	6c	0.4869(7)	0.5130(7)	0.4722(7)	0.009(2)
O4	6c	0.8337(8)	0.1662(8)	0.2463(9)	0.011(3)

FIG. 2. Structural information from single-crystal XRD. Refinement results for (a) $Mn_2Mo_3O_8$ and (b) $Fe_2Mo_3O_8$, comparing calculated and observed structure factors $|F|$; although the refinements were done using $|F|^2$, we plot our results in terms of $|F|$. (c) The azimuthal scan of $Fe_2Mo_3O_8$, showing the normalized values of intensity divided by its sigma. The (h, k, l) reflections, where l = even (odd) numbers, indicate allowed (forbidden) reflections. (d) and (e) Refined crystal-structure parameters for two compounds with the isotropic thermal parameters assuming the full occupancies.

symmetry. However, we also observed a few very weak forbidden reflections within the $P6_3mc$ space group (No. 186). If these reflections are genuinely observable nuclear Bragg reflections, then the potential space group describing these systems should be from the trigonal symmetry such as $P3m$ (No. 156) or $P3$ (No. 143), where all the observed reflections are allowed by symmetry and can be indexed. As this hypothesis can be an important result related to the interplay between the true crystal structure and electronic responses already at room temperature, we designed the azimuthal-angle measurements to understand the nature of these forbidden reflections. We chose four representative reflections covering both allowed and forbidden reflections using the $Fe_2Mo_3O_8$ single crystal according to the refection conditions for the general Wyckoff site. The results of the azimuthal scan are presented in Fig. 2(c) where we show the evolution of normalized intensity for a wide range of azimuthal angles ψ_i [$i \in [1, n]$ where n is a total number of measured angles, see Fig. 2(c)] (the label for the azimuthal angle should not be confused with the label, which we introduce later on, for the electronic wave function). Each intensity I_i was first divided by the corresponding sigma σ_i to get statistically better-defined parameters, and then (I_i/σ_i) was further normalized by the average intensity $I_{av} = \frac{1}{n}\sum_{i=1}^{n} I_i$. By comparing the normalized values of intensity $(I_i/\sigma_i)/I_{av}$, as shown in Fig. 2(c), we were able to see that the normalized values for the allowed reflections are close to the unity as expected, whereas their counterpart values from forbidden reflections are strongly fluctuating upon the azimuthal angle. This is reminiscent of the observation of forbidden reflections from the unavoidable multiple diffractions, indicating that the forbidden reflections should be excluded when determining the crystal structure. Therefore, within our experimental resolution, the given hexagonal $P6_3mc$ space group (No. 186) well describes the crystal structures of $Fe_2Mo_3O_8$.

Structural relaxations of the internal atomic coordinates for fixed experimental lattice constants have been performed using non-spin-polarized DFT and paramagnetic eDMFT methods. Structural relaxations have been performed using various starting artificial structures within subgroups of the experimental hexagonal space group $P6_3mc$ (No. 186) such as trigonal $P3m1$ (No. 156), $P3$ (No. 143), and even lower space groups up to monoclinic symmetry. In each case, the stable relaxed crystal structures were found to have the hexagonal symmetry, space group $P6_3mc$ (No. 186) within the error bar of the calculations. While DFT is a zero-temperature method, the eDMFT is a finite-temperature method. Thus eDMFT calculations were performed in the wide temperature range, and the reported results in this paper correspond to the high-temperature paramagnetic state (T_{theory} = 500 K). In Table I we report the experimental internal parameters and the corresponding theoretical parameters obtained from structural relaxations using the DFT (T = 0 K) and eDMFT (T = 500 K).

From the results presented in Table I, we see that the agreement between the experimental fractional coordinates and those obtained from the eDMFT theoretical relaxations is much better than the agreement between the experimental fractional coordinates and those obtained from the DFT theoretical relaxations. The eDMFT method gives smaller deviations (beyond the third digit with respect to the experiment) while the DFT method gives larger deviations (beyond the second digit with respect to the experiment).

Converting these discrepancies of internal structural parameters to displacements in Å along the three crystallographic directions, we find a maximum discrepancy for eDMFT (DFT) to be |0.06| (|0.27|) for $Mn_2Mo_3O_8$ and |0.06|

TABLE I. Internal structural parameters obtained experimentally at room temperature and by using various relaxations methods for $Mn_2Mo_3O_8$ (a) and $Fe_2Mo_3O_8$ (b). During the structural relaxations, the lattice parameters were kept fixed to those reported in the table.

	Experiment			eDMFT			DFT		
	X	*Y*	*Z*	*X*	*Y*	*Z*	*X*	*Y*	*Z*
(a)	$Mn_2Mo_3O_8$ $P6_3mc$ No. 186, $a = b =$ 5.79750 Å, $c =$ 10.27070 Å, $\alpha = \beta =$ 90°, $\gamma =$ 120°								
Mn1	1/3	2/3	0.0659	1/3	2/3	0.0651	1/3	2/3	0.0642
Mn2	1/3	2/3	0.6277	1/3	2/3	0.6220	1/3	2/3	0.6405
Mo	0.1459	0.8541	0.3647	0.1455	0.8544	0.3614	0.1467	0.8532	0.3646
O1	0	0	0.0000	0	0	0.0000	0	0	0.0000
O2	1/3	2/3	0.2649	1/3	2/3	0.2619	1/3	2/3	0.2536
O3	0.4878	0.5122	0.4719	0.4875	0.5125	0.4708	0.4901	0.5099	0.4978
O4	0.8356	0.1644	0.2492	0.8358	0.1641	0.2458	0.8212	0.1786	0.2521
(b)	$Fe_2Mo_3O_8$ $P6_3mc$ No. 186, $a = b =$ 5.77530 Å, $c =$ 10.05880 Å, $\alpha = \beta =$ 90°, $\gamma =$ 120°								
Fe1	1/3	2/3	0.0623	1/3	2/3	0.0625	1/3	2/3	0.0611
Fe2	1/3	2/3	0.6226	1/3	2/3	0.6233	1/3	2/3	0.6314
Mo	0.1460	0.8539	0.3603	0.1457	0.8543	0.3616	0.1474	0.8526	0.3617
O1	0	0	0.0000	0	0	0.0000	0	0	0.0000
O2	1/3	2/3	0.2584	1/3	2/3	0.2600	1/3	2/3	0.2552
O3	0.4869	0.5130	0.4722	0.4871	0.5190	0.4743	0.4881	0.5119	0.4931
O4	0.8337	0.1662	0.2463	0.8333	0.1667	0.2466	0.8228	0.1772	0.2483

(|0.21|) for $Fe_2Mo_3O_8$. We also compute the percentage difference between the experimental and theoretically obtained values in the form $\%_{\text{err}} = \frac{1}{N} \frac{|Q_{\text{theory}} - Q_{\text{expt}}| \cdot 100}{Q_{\text{expt}}}$, where Q is any of the x, y, or z fractional coordinates and the sum is taken over all N internal atomic coordinates that are allowed to displace during the structural relaxations. The computed percentage error $\%_{\text{err}}$ is 0.53% (2.3%) for $Mn_2Mo_3O_8$ versus 0.32% (1.64%) for $Fe_2Mo_3O_8$ in eDMFT (DFT), correspondingly. The obtained values of discrepancies and percentage errors show that eDMFT gives much more accurate structural degrees of freedom compared to non-spin-polarized DFT in these materials.

To better understand how these discrepancies between experimental and theoretical values of the fractional coordinates affect the properties of the local polyhedron formed between the central transition ion and the coordinating atoms (ligands), we have also computed a few quantities which are usually used to describe geometrically the coordination polyhedron. These quantities are the average bond length l_{av}(Å), polyhedral volume V (Å^3), quadratic elongation λ, and bond angle variance σ^2(deg^2). The values of these quantities can be automatically computed using the VESTA software and besides l_{av} and V, which have their usual meaning, the other two quantities are defined as follows: (I) quadratic elongation λ is a dimensionless quantity and gives a quantitative measure of the polyhedral distortion, independent of the effective size of the polyhedron $\lambda = \frac{1}{n} \sum_{i=1}^{n} (\frac{l_i}{l_0})^2$, where n is the coordination number of the central atom, l_i is the distance from the central atom to the ith coordinating atom, and l_0 is the center-to-vertex distance of a regular polyhedron of the same volume (a regular polyhedron has a quadratic elongation of 1, whereas distorted polyhedra have values greater than 1); (II) bond angle variance gives a measure of the distortion of the intrapolyhedral bond angles from the ideal polyhedron $\sigma^2 = \frac{1}{m-1} \sum_{i=1}^{m} (\theta_i - \theta_0)^2$, where m is the number of bond angles [3/2·(number of faces in the polyhedron)], θ_i is the ith bond angle, and θ_0 is the ideal bond angle for a regular polyhedron (θ_0 is 90° for an octahedron and 109°28 for a tetrahedron). Bond angle variance is zero for a regular polyhedron and positive for a distorted polyhedron. The average bond length, polyhedron volume, quadratic elongation, and bond angle variance are scalar quantities, so they provide no information about the geometry of polyhedral distortions, but they can be used to quantitatively compare the agreement between the experimentally determined and theoretically obtained fractional coordinates.

In Figs. 3(a) and 3(b) we give the values of the above-mentioned quantities for $M_2Mo_3O_8$, computed based on fractional coordinates obtained from the experiment, eDMFT, and DFT relaxations. Besides, we give the percentage error between the experimental and theoretically obtained values in the form $\%_{\text{err}} = \frac{|Q_{\text{theory}} - Q_{\text{expt}}| \cdot 100}{Q_{\text{expt}}}$, where Q can be any of the quantities, l_{av}, V, λ, and σ^2. The computed percentage error ($\%_{\text{err}}$) of the quantities mentioned above, is orders of magnitude smaller for eDMFT than DFT, see Figs 3(a) and 3(b).

B. HT electronic properties: Experiment and theory

To confirm the insulating properties of the $M_2Mo_3O_8$ compounds, we have performed ellipsometric measurements of the pseudodielectric function in the *ab* plane and along the *c* axis, see Fig. 4. Our data show that both compounds are insulators with tangible across-the-gap transitions starting at 8700 cm^{-1} (1.08 eV) for $Fe_2Mo_3O_8$ and 11 800 cm^{-1} (1.46 eV) for $Mn_2Mo_3O_8$ compounds. As was discussed in Sec. III A, the eDMFT method better reproduces the structural properties than the DFT method does. Now we will present the electronic properties obtained by these two methods. Figures 3(c)–3(d) and Figs. 3(e) and 3(f) show the total density

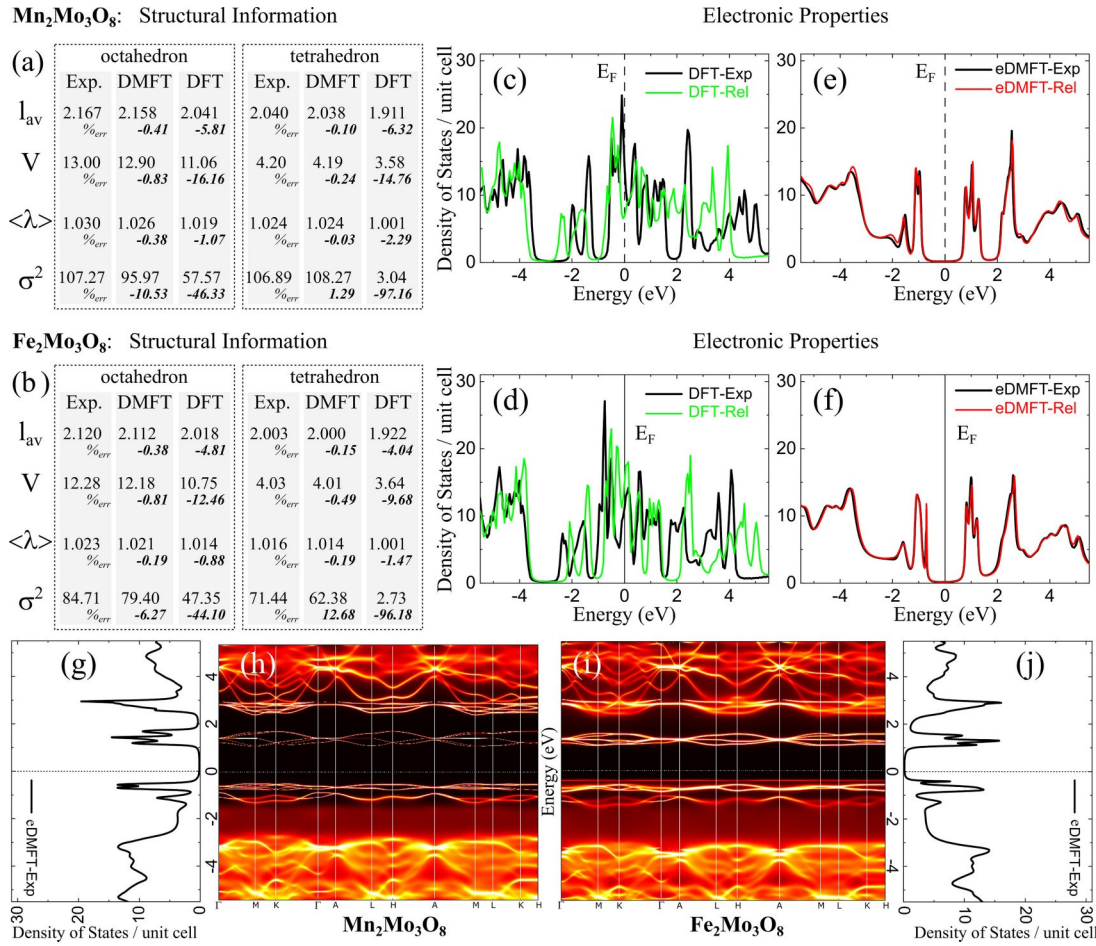

FIG. 3. Structural and electronic properties of $M_2Mo_3O_8$. (a) and (b) The comparison between the experiment and theoretical methods for various quantities defined in Sec. III for the transition-metal polyhedron (MO_6 and MO_4); $\%_{\mathrm{err}}$ represents the percentage error (bold numbers) between the experiment and theory. (c) and (d) The total density of states obtained by using the DFT method for the experimental structures (black) and for those obtained by using structural relaxations of internal parameters in DFT (green). (e) and (f) The total density of states obtained by using the eDMFT method for the experimental structures (black) and for those obtained by using structural relaxations of internal parameters in eDMFT (red). (h) and (i) Spectral functions. (g) and (j) Repetition of (e) and (f).

of states obtained by the DFT and the eDMFT methods, respectively. As expected, DFT gives a metallic state, but eDMFT gives an insulating state with gap values ~1.2 eV for $Fe_2Mo_3O_8$ and ~1.4 eV from $Mn_2Mo_3O_8$ [see Figs. 3(h)–3(i)], which are close to the experimental values of 1.08 and 1.46 eV, respectively. If we also compute the total density of states for the relaxed crystal structures within the DFT and eDMFT methods and compare it to the density of states obtained using the experimental structure, we see that within the DFT method the two electronic structures are different but for the eDMFT method we get very similar total density of states for both compounds. The details of the electronic structures obtained by the eDMFT will be published elsewhere.

C. LT vs HT structural properties: Infrared phonon spectra

Figure 5 shows far-infrared reflectivity spectra dominated by the phonon modes for $Fe_2Mo_3O_8$ and $Mn_2Mo_3O_8$ compounds measured for two polarizations of the incident light $e||c$ and $e \perp c$ at 85 and 5 K, i.e., above and below magnetic ordering temperatures in these compounds. To determine parameters of the phonon modes, reflectivity spectra were fitted using parametrization of the dielectric function with Drude-Lorentz oscillators [42] and the Kramers-Kronig transformation as implemented in the REFFIT code [43]. In this framework the dielectric function is parametrized as follows:

$$\varepsilon_{ab} = \varepsilon_{\infty,\,ab} + \sum_{i=1}^{n} \frac{\omega_{i,ab}^2 S_{i,ab}}{\omega_{i,ab}^2 - \omega^2 - i\gamma_{i,ab}\omega},$$

$$\varepsilon_{c} = \varepsilon_{\infty,\,c} + \sum_{j=1}^{m} \frac{\omega_{j,c}^2 S_{j,c}}{\omega_{j,c}^2 - \omega^2 - i\gamma_{j,c}\omega},$$

where $\omega_{i(j),ab(c)}$, $S_{i(j)ab(c)}$, and $\gamma_{i(j)ab(c)}$ are transverse optical (TO) frequency, oscillator strength, and inhomogeneous broadening of the ith (jth) phonon mode polarized along the ab plane (c axis), and $\varepsilon_{\infty,\,ab(c)}$ is the value of the dielectric function along the ab plane (c axis) at frequencies higher than that of the highest-energy phonon mode. The extracted frequencies of the phonon modes are listed in Table II. Above the

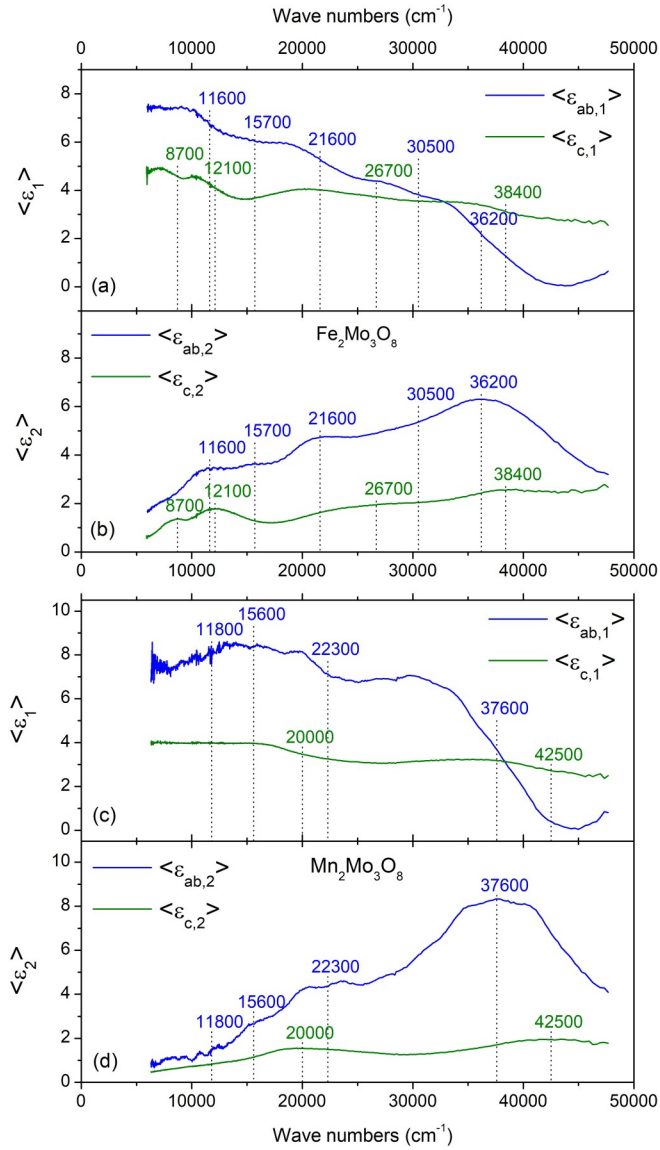

FIG. 4. Spectra of real and imaginary parts of pseudodielectric function of (a) and (b) $Fe_2Mo_3O_8$ and (c) and (d) $Mn_2Mo_3O_8$ in the *ab* plane (blue curve) and along the *c* axis (olive curve) in the region of electronic $d - d$ transitions in Fe^{2+} and Mo^{4+} ions at $T = 300$ K.

magnetic ordering temperature, there are a total of 19 (22) IR active phonon modes observed for $Fe_2Mo_3O_8$ ($Mn_2Mo_3O_8$) compound, 10 (9) being polarized along the *c* axis and 9 (13) in the *ab* plane (see Table II and spectra in Fig. 5 for $T = 85$ K). Below the magnetic ordering temperature, the number of observed phonon modes does not change for the Mn compound, while three new peaks at 270, 429, and 470 cm^{-1} arise in $e \perp c$ spectra for the Fe compound (see spectra in Fig. 5 for $T = 5$ K). The inset in Fig. 5(a) shows the temperature dependence of new peaks at 429 and 470 cm^{-1} in more detail. These peaks appear and reach nearly full intensity as the temperature lowers from 70 to 50 K, and thus their appearance is associated with the onset of phase transition at $T_N = 60$ K rather than with a continuous narrowing of the peaks' width due to a gradual temperature decrease from 300 to 5 K.

D. LT vs HT structural properties: Raman phonon spectra

Spectra of the optical phonons in the same $Fe_2Mo_3O_8$ and $Mn_2Mo_3O_8$ crystals have been also studied using Raman scattering. Several backscattering configurations were utilized: $x(z, z)\bar{x}$, $x(z, y)\bar{x}$, $z(x, y)\bar{z}$, and $z(x, x)\bar{z}$, where $x||a$, $z||c$, $y\perp(x, z)$, the first and the last symbols in Raman notations correspond to the *k*-vector direction for the incident and scattered light, whereas symbols in brackets correspond to the polarization direction of the incident and scattered light. In these geometries the following mode symmetries should become accessible [44] in the $P6_3mc$ crystal structure of $M_2Mo_3O_8$ crystals: A_1, E_1, E_2, and $A_1 + E_2$ (see Table IV), as the in-plane *x* and *y* axes could not be distinguished for a hexagonal crystal. As shown in Fig. 6, the experimental Raman spectra are highly polarized, which allowed us to identify positions of the A_1, E_1, and E_2 phonon modes. There are a total of 31 (34) Raman active modes observed for $Fe_2Mo_3O_8$ ($Mn_2Mo_3O_8$) at 85 K, among which are 9(10) A_1 modes, 11(12) E_1 modes, and 11(12) E_2 modes. As the temperature is lowered and the Fe compound undergoes the magnetic ordering, several new lines appear (see Fig. 7). In particular, two new A_1 modes at 232 and 852 cm^{-1}, one new E_1 mode at 748 cm^{-1}, and five new E_2 modes at 127, 158, 193, 224, and 253 cm^{-1} are observed in the spectra of $Fe_2Mo_3O_8$ at 5 K. Both new A_1 modes at 232 and 852 cm^{-1} are observed in the IR spectra at 85 K, so they are likely high-temperature modes that are just too weak in the Raman spectra at 85 K to be resolved. We shall examine whether new modes correspond to phonons or electronic $d - d$ transitions in Fe^{2+} ions, as the latter are expected to overlap with the phonon spectra in the $Fe_2Mo_3O_8$ compound [45]. The number of modes observed for the Mn compound does not change between 5 and 300 K, i.e., above and below T_C(Mn) = 41 K. The positions and symmetries of the identified Raman active modes for $Fe_2Mo_3O_8$ and $Mn_2Mo_3O_8$ at both 85 and 5 K are summarized in Table II. As expected for the polar structure of the studied compounds, there is a good agreement between positions of IR- and Raman-active modes barring several modes of the E_1 symmetry in the $Fe_2Mo_3O_8$ compound. In the frequency range of 860 – 1300 cm^{-1}, we observe weak overtones for the optical phonons positioned at 1214 cm^{-1} for $Fe_2Mo_3O_8$ and at 1103, 1200, and 1220 cm^{-1} for $Mn_2Mo_3O_8$, which correspond to two-phonon Raman scattering.

E. HT: First principle phonon calculations

We have shown so far that the eDMFT method is in a better agreement with the experimental data when it comes to the fractional atomic coordinates. Also, eDMFT can capture the insulating state of these materials while DFT gives a metallic state. It is well known that in many cases even if DFT cannot fully explain the ground state electronic properties, the computed phonons are in good agreement with the experimentally obtained phonons. In this respect, we computed the phonon modes at the DFT level for the high-temperature $P6_3mc$ structure of $M_2Mo_3O_8$ (M = Fe, Mn) and the obtained values for the mode frequencies are given in Table II side by side with the experimental values obtained from the IR and Raman measurements. To quantify the agreement between the calculated and measured phonon frequencies, we are computing the

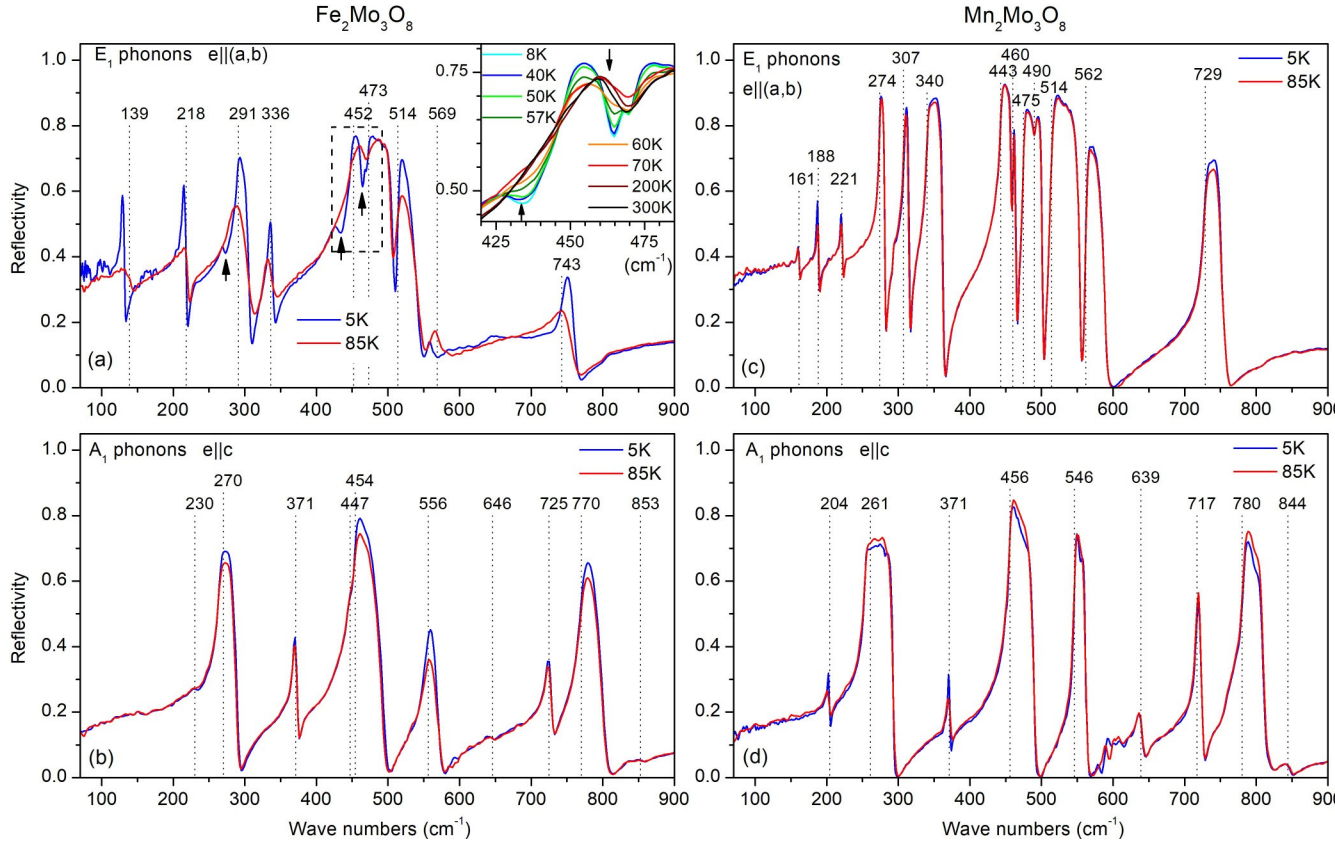

FIG. 5. Reflectivity spectra of (a) and (b) $Fe_2Mo_3O_8$ and (c) and (d) $Mn_2Mo_3O_8$ in (a) and (c) $e \perp c$ and (b) and (d) $e \| c$ polarizations at 85 (red line) and 5 K (blue line). Three new lines that appear in the $e \perp c$ spectra of $Fe_2Mo_3O_8$ below the magnetic ordering temperature of Fe spins T_N(Fe) = 60 K are shown with arrows in (a). The inset in (a) shows the temperature evolution of the new modes at 429 and 470 cm^{-1}, which appear below T_N(Fe) = 60 K.

percentage error $\%_{\text{err}} = \frac{1}{N}\sum_{i=1}^{N}\frac{|\omega^i_{\text{expt}}-\omega^i_{\text{theory}}|}{\omega^i_{\text{expt}}}\cdot 100$, which expresses as a percentage the difference between the computed and measured values of the phonon frequencies (N is the total number of measured phonon frequencies, ω^i_{expt} and ω^i_{theory} are the experimental and computed phonon frequencies). A percentage error very close to zero means that there is a very good agreement between the theory and the experiment. Computing the percentage error between the experimental and calculated frequencies of the IR phonon modes, we obtained a percentage error of 5.3% and 3.8% for the Mn and Fe compounds, correspondingly. Another way to compare the computed and measured phonon frequencies is by calculating the mean value $\omega_{\text{mean}} = \frac{1}{M}\sum_{i=1}^{M}\omega_i$, where M runs over all computed or measured phonon frequencies. The mean values for the IR phonon frequencies obtained in experiment vs theory are 430 vs 421 cm^{-1} for the Mn compound and 444 vs 421 cm^{-1} for the Fe compound. If we compute the percentage error for the mean values, we obtain 2.1% for Mn and 5.2% for Fe compounds. From the calculated values, we see that the overall agreement between the theory and experiment is within a few percent, which we might consider as a good one.

F. Temperature-dependent electronic transitions in Fe^{2+} ions in $Fe_2Mo_3O_8$

Figure 8 shows IR reflectivity spectra of $Fe_2Mo_3O_8$ in a wide spectral range from 100 to 4000 cm^{-1}, which covers IR active phonons located in the 100 – 800 cm^{-1} region, a broad spectral feature at ~ 3000 cm^{-1} [Fig. 8(a)], and a group

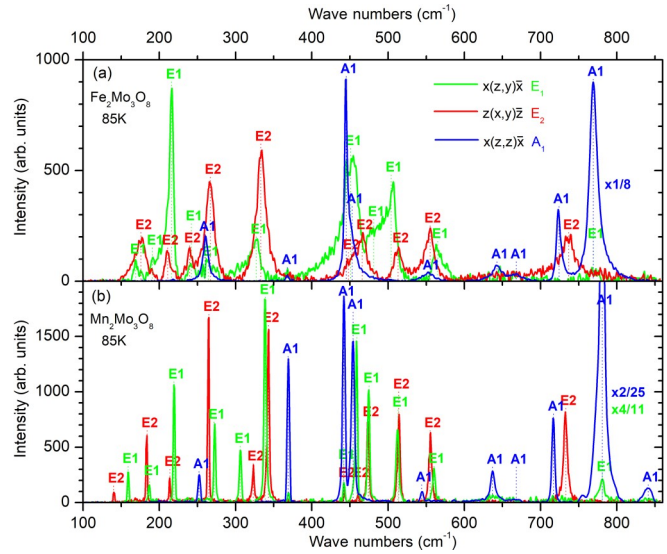

FIG. 6. Raman spectra of (a) $Fe_2Mo_3O_8$ and (b) $Mn_2Mo_3O_8$ measured above the magnetic ordering temperature of Fe (Mn) spins in three complementary scattering geometries: $x(z, y)\bar{x}$ (green lines), $z(x, y)\bar{z}$(red lines), and $x(z, z)\bar{x}$ (blue lines), where $x \| a$, $z \| c$, and $y \perp (x, z)$. The phonon peaks are labeled according to their irreducible representations of the $P6_3mc$ space group.

TABLE II. Frequencies and symmetries of the experimental IR- and Raman-active phonons at 85 and 5 K, i.e., above and below the magnetic ordering temperature of M spins, as well as calculated (Calc.) phonons in $M_2Mo_3O_8$ (M = Fe, Mn). All phonon frequencies are in cm^{-1}. $\varepsilon_{\infty,\ ab(c)}$ is the value of the dielectric function along the ab plane (c axis) at frequencies higher than that of the highest-energy phonon mode and is listed at the bottom. Modes which appear in the spectra only below the magnetic ordering temperature of M spins are marked with LT. Modes with energies which are close to calculated electronic energy levels of Fe^{2+} ions and which may be related to electronic transitions rather than phonons are marked with CF.

		A_1					E_1					E_2		
		IR		Raman		Calc.	IR		Raman		Calc.	Raman		Calc.
M		85 K	5 K	85 K	5 K	300 K	85 K	5 K	85 K	5 K	300 K	85 K	5 K	300 K
Fe[a]	1	230	230		232	232	139	129					127^{LT}	
	2	270	269	260	263	267			169	179			158^{LT}	
	3	371	370	368	369	362			191	194		176	180	147
	4	447	447	445	446	446	218	214	216	213	211		193^{LT}	
	5	454	453	453	453	514			242	242	264	211	205	204
	6	556	556	553	553	620		$270^{LT,CF}$	264	253	268		$224^{LT,CF}$	
	7	646	646	643	644		291	292			281	240	$253^{LT,CF}$	240
	8			668	668		336	336	327	333	338	267	268	278
	9	725	725	724	724	728		429^{LT}				328	328	
	10	770	770	769	771	792	452	452	451	454	451	333	334	367
	11	853	853		852	838		$470^{LT,CF}$				448	448	433
	12						473	472	481	487	470	466	469	464
	13						514	515	504	500	506	513	513	508
											549			
	14						569	558	565	575	559	555	555	548
											588			560
											660			572
														665
	15									$748^{LT,CF}$		737	746	802
							743	750	769	769	803			
Mn[b]	1	204	204			240	161	161	159	159		140	140	141
	2	261	262	252	252	296	188	188	187	186		184	183	214
	3	371	370	369	369	344	221	221	219	219	210	214	214	230
						366								
	4			442	442		274	274	272	272	248	265	265	264
											271			
	5	456	456	454	454	454	307	308	306	307	301	323	324	308
	6	546	547	544	544	504	340	341	339	339	397	343	343	379
	7	639	640	637	637	560	443	443	442	442	410	442	442	423
														430
	8			668	668		460	460	459	459	434	461	461	467
	9	717	718	717	717	727	475	476	475	475	470	474	474	485
	10	780	781	781	781	759	490	490			483	514	514	518
	11	844	842	841	841		514	513	513	513	523	555	555	543
	12						562	561	560	560	539	733	733	694
	13						729	729			690			
	14								781	781				

[a]Fe: $\varepsilon_{\infty,\ ab} = 4{\cdot}7, \varepsilon_{\infty,\ c} = 5{\cdot}0$.
[b]Mn: $\varepsilon_{\infty,\ ab} = 6{\cdot}1, \varepsilon_{\infty,\ c} = 4{\cdot}0$.

of weak narrow lines in the 3400 − 3500 cm^{-1} region. As temperature increases from 5 to 85 K, most of the narrow lines in 3400− 3500 cm^{-1} region vanish, while the strong and broad feature at ~ 3000 cm^{-1} redshifts by several hundred wave numbers.

Figures 9(a)–9(d) show in more detail temperature dependence of spectral lines in the 2150 − 3600 cm^{-1} range measured for $Fe_2Mo_3O_8$ (two different samples referred to as sample 1 and sample 2 in the text below), $FeZnMo_3O_8$ and $Mn_2Mo_3O_8$ single crystals. In this spectral range, the most prominent feature is the broad line at ~ 3000 cm^{-1} observed in $Fe_2Mo_3O_8$ sample 1 [see Fig. 9(a)]. As temperature increases, the line redshifts by ~ 400 cm^{-1} [see inset in Fig. 9(a)] and gradually decreases in intensity but does not vanish up to room temperature. To explore the behavior of the line in more detail, we measured the same spectra from a

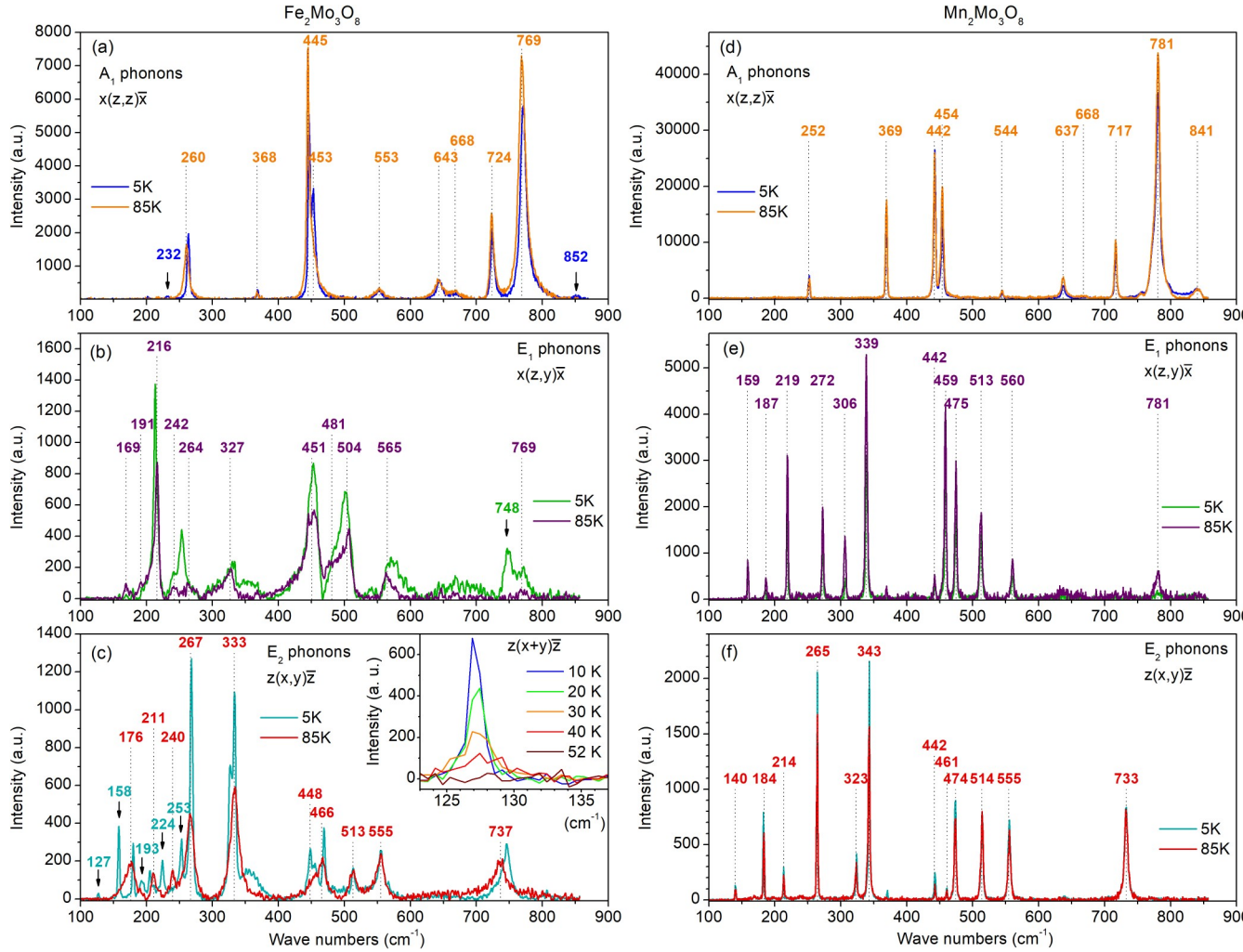

FIG. 7. Raman spectra of phonon modes in (a)–(c) $Fe_2Mo_3O_8$ and (d)–(f) $Mn_2Mo_3O_8$ measured in (a) and (d) $x(z, z)\bar{x}$, (b) and (e) $x(z, y)\bar{x}$, and (c) and (f) $z(x, y)\bar{z}$ configurations at 85 and 5 K, i.e., above and below the magnetic ordering temperature of Fe (Mn) spins. In the Raman notations the following Cartesian coordinate system is used: $x \| a$, $z \| c$, and $y \perp (x, z)$. New lines which appear in the spectra of $Fe_2Mo_3O_8$ below the magnetic ordering temperature T_N(Fe) = 60 K are marked with arrows in (a)–(c). The inset in (c) shows the temperature evolution of the new mode at 127 cm^{-1}, which appears below T_N(Fe) = 60 K.

different (presumably better quality) $Fe_2Mo_3O_8$ single crystal [sample 2; see Fig. 9(b)]. Interestingly, the line is absent in the spectra of $Fe_2Mo_3O_8$ sample 2. It is also absent in the spectra of $Mn_2Mo_3O_8$ single crystal [see Fig. 9(d)] but present, although to a lesser degree, in the spectra of $FeZnMo_3O_8$ sample [see Fig. 9(c)]. The inconsistency in observation of this line in the spectra of $Fe_2Mo_3O_8$ samples suggests that it is likely an artifact of the measurements, which may be related to the quality of the samples.

The group of narrow lines in the 3400 – 3500 cm^{-1} region was observed for both $Fe_2Mo_3O_8$ samples but absent in the spectra of $FeZnMo_3O_8$ and $Mn_2Mo_3O_8$ samples. As was shown in Ref. [9], Zn^{2+} ions prefer to substitute Fe^{2+} ions in the tetrahedral (t) coordination. Previous spectroscopic study [46] of Fe-doped ZnS, CdTe, and $MgAl_2O_4$ compounds has shown that $d - d$ electronic transitions in Fe^{2+} (t) ions fall into the 3000 – 4000 cm^{-1} energy range. Thus, we attribute the observed lines to the $d - d$ electronic transitions in Fe^{2+} (t) ions.

Spectra in Fig. 9 also manifest a broad spectral feature at 3250 cm^{-1}. It is observed in the spectra of $Fe_2Mo_3O_8$ sample 2 [Fig. 9(b)] and $Mn_2Mo_3O_8$ [Fig. 9(d)] compounds, and it is also seen, although less clearly, in the spectra of $Fe_2Mo_3O_8$ sample 1 [Fig. 9(a)] and $FeZnMo_3O_8$ [Fig. 9(c)]. Since both $Mn_2Mo_3O_8$ and $Fe_2Mo_3O_8$ samples manifest this feature, we conclude that it is not related to $d - d$ electronic transitions in Fe^{2+} ions.

Figure 10 shows the temperature dependence of IR and Raman spectra of Fe^{2+} (t) $d - d$ electronic transitions measured in different optical configurations. The positions of electronic transitions have been identified and summarized in Table III for T = 5 K. With increasing temperature, intensities of the Raman-active transitions gradually decrease until they completely vanish above 52 K, i.e., near the magnetic ordering temperature T_N(Fe) = 60 K of $Fe_2Mo_3O_8$ [see Fig. 10(c)]. Infrared-active modes observed in Figs. 10(a) and 10(b) behave in a similar way: they decrease in intensity with the temperature increase and are practically indistinguishable in

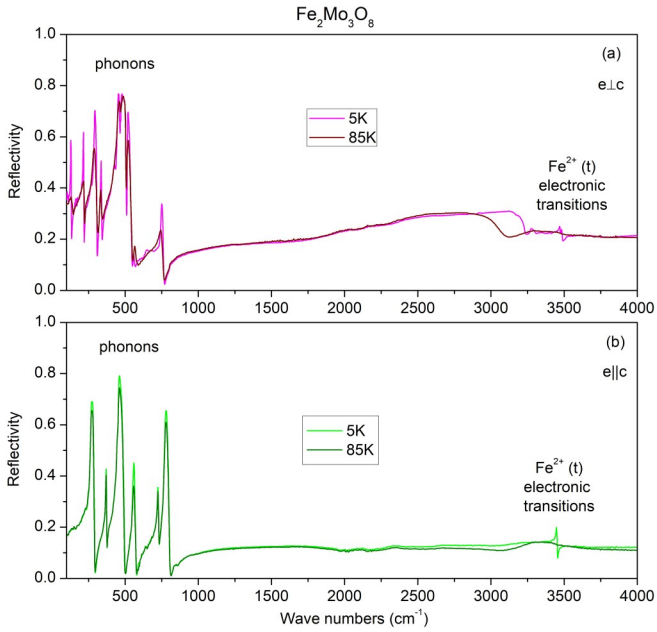

FIG. 8. Infrared reflectivity spectra in the region of phonon modes and electronic $d - d$ transitions in Fe^{2+} ions in tetrahedral (t) coordination in $Fe_2Mo_3O_8$ crystal in (a) $e \perp c$ and (b) $e \| c$ polarizations at 85 and 5 K.

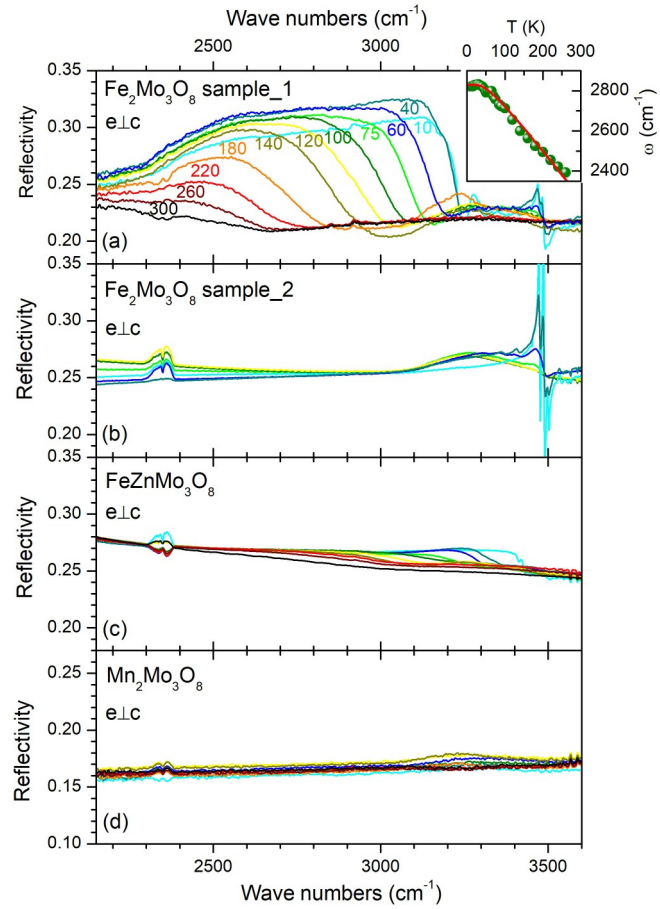

FIG. 9. Infrared reflectivity spectra of (a) $Fe_2Mo_3O_8$ sample 1, (b) $Fe_2Mo_3O_8$ sample 2, (c) $FeZnMo_3O_8$, and (d) $Mn_2Mo_3O_8$ in $e \perp c$ polarization at temperatures between 5 and 300 K. The inset in (a) shows the temperature dependence of the position of the broad peak at ~ 2800 cm^{-1}; the red line is a guide for the eye.

the spectra above 70 K. At the same time, as we increase the temperature, two new infrared-active modes at 3358 and 3405 cm^{-1} gradually appear to the low energy side of the infrared modes observed at $T = 5$ K (see Fig. 11). Such behavior is typical for the transitions originating from the first excited energy levels, which become populated with the temperature increase. The intensity of the modes reaches a maximum at $T \sim 40$ K above which the lines broaden, and their intensity decreases until they disappear from the spectra above 70 K. The broad feature at 3250 cm^{-1} marked with an asterisk in Fig. 11 is the same feature as in Figs. 9(a)–9(d) and is not related to $d - d$ electronic transitions in Fe^{2+} ions.

G. Crystal-field calculations

Several new modes which appear in the far-infrared and Raman spectra of $Fe_2Mo_3O_8$ below the magnetic ordering temperature $T_N = 60$ K can be related to either phonons or $d - d$ electronic transitions in Fe^{2+} ions. Crystal-field calculations can predict the energy levels of Fe^{2+} ions and thus help us to separate the electronic and vibrational contributions to the spectra. Such calculations have been reported for $Fe_2Mo_3O_8$ [45] where the parameters of the model have been tuned to explain Mössbauer data. In the current study we attempt to improve upon the model suggested in Ref. [45] by fitting the model parameters to the expanded experimental database, which includes our data on electronic transitions in Fe^{2+} (t) ions in 3400 – 3500 cm^{-1} range as well as recent suggestions [12,13] on energy level(s) of Fe^{2+} (o) ions in the THz range.

We start with the description of the model. To induce a transition between two energy levels in the solid, the energy of the photon ($h\nu$) should be close to the energy difference between the levels ($E = h\nu$). However, even if the photon has the proper energy, the intrinsic probabilities of transition depend on many details of the solid. The mechanism, by which the photon causes the solid to undergo a transition between two levels, can be described in terms of the eigenfunctions of the solid Hamiltonian. In general, the experimentally observed intensity of a transition is proportional to the square of a matrix elements $|\langle \psi_f(r, R_f)|\mathbf{M}|\psi_i(r, R_i)\rangle|^2$, where $|\psi_i(r, R_i)\rangle$ and $|\psi_f(r, R_f)\rangle$ are eigenfunctions of the Hamiltonian, r are electrons coordinates, R are nuclei coordinates, and $\mathbf{M}$ is the corresponding operator associated with the perturbing potential of the photon which drives a transition between the initial $|\psi_i(r, R_i)\rangle$ and the final $|\psi_f(r, R_f)\rangle$ eigenfunctions [47]. The eigenfunctions $|\psi(r, R)\rangle$ depend on the coordinates of the electrons r and of the nucleus R in the solid. Because the electrons move much more rapidly than the nuclei, we can treat the nuclear and electronic motions separately (Born-Oppenheimer approximation) and write the eigenfunctions as a product of the electronic eigenfunction $|\ (r, R)\rangle$ (which depends on the nuclear coordinates R only in a parametric manner) and the nuclear eigenfunction $|\chi(R)\rangle$, $|\psi(r, R)\rangle = |\ (r, R)\rangle|\chi\ (R)\rangle$. As a result, we can describe the electronic and vibrational/rotational energy levels independently. We note that each electronic state is determined by

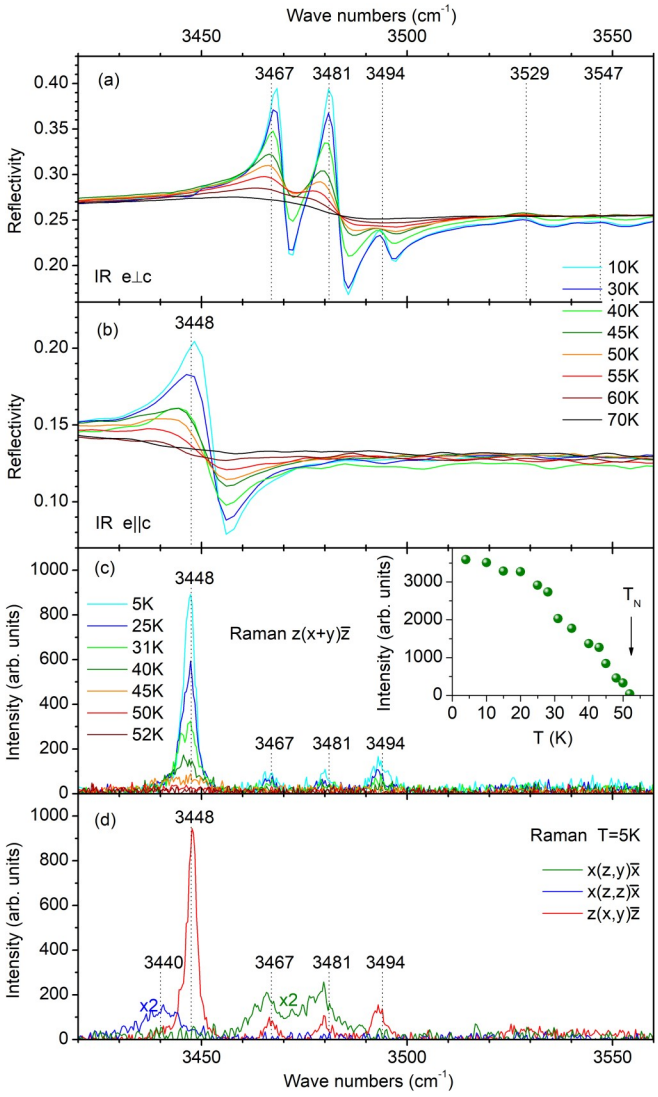

FIG. 10. (a) and (b) Reflectivity spectra of $d-d$ crystal-field transitions in Fe^{2+} ions in $Fe_2Mo_3O_8$ at different temperatures in (a) $e\perp c$ and (b) $e\,||c$ polarizations. (c) and (d) Raman spectra of $d-d$ crystal-field transitions in Fe^{2+} ions in (c) $z(x+y)\bar{z}$ configuration at different temperatures and (d) $x(z,y)\bar{x}$ (green curve), $x(z,z)\bar{x}$ (blue curve), and $z(x,y)\bar{z}$ (red curve) configurations at 5 K, where $x||a$, $z||c$, and $y\perp(x,z)$. Inset in (c) shows temperature dependence of the intensity of 3448 cm^{-1} Raman mode.

an electronic eigenfunction $|(r,R_0)$ with the corresponding energy eigenvalue $E_e(R_0)$, which depends on a fixed set of nuclear coordinates R_0 as a parameter. A plot of $E_e(R)$ gives rise to potential energy surface which is further used in obtaining the nuclear eigenfunctions $|\chi(R)$ and hence the vibrational/rotational energies $E_{\rm vib}(R)/E_{\rm rot}(R)$. In conclusion, we can say that each electronic state has its own potential surface characterized by the equilibrium nuclear coordinates R_0, and associated with it several vibrational levels which themselves contain many rotational sublevels. Thus, during an electronic transition, there is also a change in both vibrational and rotational levels [48]. If the electronic transitions are driven by an operator that depends only on the

TABLE III. Frequencies $E(cm^{-1})$ of the IR- and Raman-active $d-d$ electronic transitions in Fe^{2+} ions in tetrahedral (t) coordination in $Fe_2Mo_3O_8$ at 5 K along with optical configurations in which they were observed. Transitions are labeled as $i\rightarrow j$, where i and j are ordinal indices of Fe^{2+} (t) energy levels obtained from the crystal-field calculations (see Table V).

		IR		Raman			
Transition	$E(cm^{-1})$	$e\perp c$	$e\|\|c$	$x(z,z)\bar{x}$	$x(z,y)\bar{x}$	$z(x,y)\bar{z}$	$z(x,x)\bar{z}$
$3\rightarrow 16$	3358	•					
$2\rightarrow 18$	3405	•					
$1\rightarrow 17$	3448		•			•	•
$1\rightarrow 19$	3467	•			•	•	•
$1\rightarrow 21$	3481	•			•	•	•
$1\rightarrow 22$	3494	•				•	•
$1\rightarrow 24$	3529	•					
$1\rightarrow 25$	3547	•					

electronic coordinates $\mathbf{M}(r)$, we can write

$$|\psi_f(r,R_f)|\mathbf{M}|\psi_i(r,R_i)|^2 = |\ f(r,R_f)|\mathbf{M}|\ i(r,R_i)|^2\ \chi_b\ R_f^b\ \chi_a\ R_i^a\ ^2,$$

where the second term is called Franck-Condon factor and $|\chi_a(R_i^a)$ and $|\chi_b(R_f^b)$ are the vibrational eigenfunctions associated with the initial $|\ i(r,R_i)$ and the final $|\ f(r,R_f)$ electronic states. Qualitatively, we can understand the matrix elements as a transition that occurs from the lowest vibrational state $|\chi_a(R_{i,0}^a)$ of the electronic ground state $|\ i(r,R_{i,0})$ to the vibrational state $|\chi_b(R_f^b)$ of the excited electronic state $|\ f(r,R_{f,0})$ that it most resembles in terms of the vibrational eigenfunction $|\chi_a(R_{i,0}^a)$ [in other words, we can say that

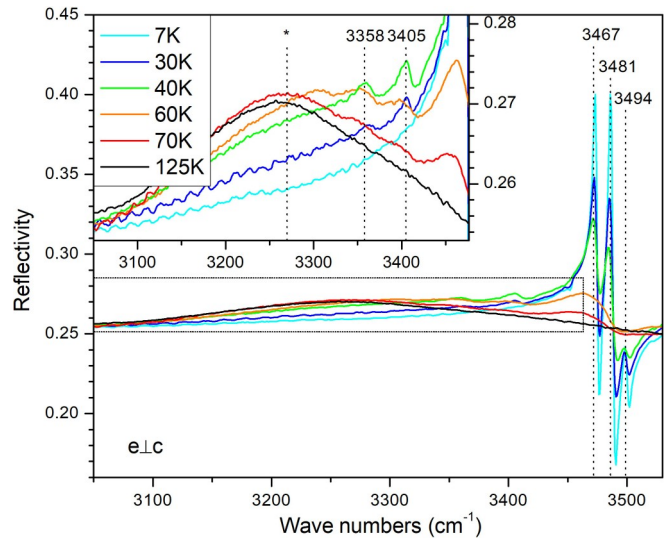

FIG. 11. Reflectivity spectra of $d-d$ crystal-field transitions in Fe^{2+} ions in tetrahedral (t) coordination in $Fe_2Mo_3O_8$ at different temperatures in $e\perp c$ polarization. Inset is a zoom of the rectangular region showing temperature-dependent spectra of satellite lines at 3358 and 3405 cm^{-1} appearing with temperature increase at the low energy side of the Fe^{2+} (t) $d-d$ transitions observed at 3467, 3481, and 3494 cm^{-1} at $T=5$ K.

the vibrational eigenfunctions $|\chi_a(R^a_{i,0})$ and $|\chi_b(R^b_f)$, associated with the initial $|\ _i(r, R_{i,0})$ and final electronic states $|\ _f(r, R_{f,0})$, must overlap]. Besides the electronic matrix elements $|\ _f(r, R_f)|\mathbf{M}|\ _i(r, R_i)|^2$, an important factor in the intensity of an electronic transition is the overlap of the vibrational eigenfunctions, which is maximum when a vertical transition occurs between vibrational levels of the upper and lower electronic states at which the vibrational wave functions have maximum values, which happens for $|\chi_a(R^a_{i,0})$ and $|\chi_b(R^b_{i,0})$ [49]. Calculating matrix elements associated with an electronic transition is a complex task, but finding out if they have a finite value is an easier task, and can be achieved using the group theory. For any atom, molecule, or solid with a given symmetry group, an important property of the Hamiltonian is that it must not change if any symmetry transformation from the symmetry group is applied onto it. Due to this property, the eigenfunctions $|\ (r, R)$ of the Hamiltonian transform the same way as the irreducible representations of the symmetry group, thus the irreducible representations are used as labels for the eigenfunctions $|\ (r, R)$, . If the initial $|\ _i(r, R_i)$ and the final $|\ _f(r, R_f)$ eigenfunctions and the transition operator $\mathbf{M}$ transform as $_i$, $_f$, and $_M$ then $|\ _f(r, R_f)|\mathbf{M}|\ _i(r, R_i)|^2 = 0$ (the electronic transition is allowed) only if the direct product $_f^* \otimes\ _M \otimes\ _i$ contains the totally symmetric representation $_1$, otherwise $|\ _f(r, R_f)|\mathbf{M}|\ _i(r, R_i)|^2 = 0$ (the electronic transition is forbidden), where the * symbol stands for a complex conjugate operation in the case where the irreducible representation has complex characters. For the case of infrared and Raman spectra, the transition operators $\mathbf{M}$ are the dipole moment $\mathbf{d}$ (a vector operator) and the polarizability $\boldsymbol{\alpha}$ (a tensor operator), respectively [48]. The dipole moment operator has components $\mathbf{d}_x$, $\mathbf{d}_y$, and $\mathbf{d}_z$, whose symmetry properties are the same as those of x, y, and z functions listed in the character table of the symmetry group. The polarizability operator is symmetric tensor having six independent components, $\boldsymbol{\alpha}_{ij}$ $(i, j = x, y, z)$ whose symmetry properties are the same as those of quadratic functions constructed by binary products of x, y, and z (i.e., x^2, y^2, z^2, xy, yz, and xz) or combinations of binary products (i.e., $x^2 - y^2$, etc). For an infrared transition to be allowed, only one of the three components $\mathbf{d}_x$, $\mathbf{d}_y$, and $\mathbf{d}_z$ has to give a nonzero matrix element, whereas for a Raman transition—only one of the six components $\boldsymbol{\alpha}_{ij}$ has to give a nonzero matrix element.

To find out the eigenfunctions of the d electrons for the Fe^{2+} ions inside $Fe_2Mo_3O_6$, one must write down (I) the perturbation Hamiltonian which acts on the d electrons of the Fe^{2+} ions when the ions are placed inside a solid such as $Fe_2Mo_3O_8$ and (II) the electronic eigenfunctions of the d electrons for the free Fe^{2+} ions on which the perturbation Hamiltonian acts.

(I) The perturbation Hamiltonian is based on the crystal-field theory, as developed in Ref. [45], and has the following form:

$$\mathbf{H} = \mathbf{H}_{\mathrm{CF}} + \mathbf{H}_{\mathrm{SO}} + \mathbf{H}_{\mathrm{SS}} + \mathbf{H}_{\mathrm{mol}},$$

where $\mathbf{H}_{\mathrm{CF}}$ is the crystal field, $\mathbf{H}_{\mathrm{SO}}$ is the spin-orbit, $\mathbf{H}_{\mathrm{SS}}$ is the spin-spin [50,51], and $\mathbf{H}_{\mathrm{mol}}$ is the molecular field Hamiltonian operators with the following forms:

$$\mathbf{H}_{\mathrm{CF}} = B^0_2\mathbf{O}^0_2 + B^0_4\mathbf{O}^0_4 + B^3_4\mathbf{O}^3_4,$$
$$\mathbf{H}_{\mathrm{SO}} = \lambda\,\mathbf{LS},$$
$$\mathbf{H}_{\mathrm{SS}} = -\rho\ \ (\mathbf{LS})^2 + \tfrac{1}{2}\mathbf{LS} - \tfrac{1}{3}L(L+1)S(S+1)\ ,$$
$$\mathbf{H}_{\mathrm{mol}} = gH_m\mu_B\mathbf{S},$$

where $\mathbf{L} = \ _i\mathbf{l}_i$ and $\mathbf{S} = \ _i\mathbf{s}_i$ are the total orbital and spin operators, $\mathbf{l}_i$ and $\mathbf{s}_i$ are the orbital and spin operators of individual electrons, and $\mathbf{O}^0_2(\mathbf{L})$, $\mathbf{O}^0_4(\mathbf{L})$, and $\mathbf{O}^3_4(\mathbf{L})$ are Stevens operators [37,38]. The other parameters in these equations, such as B^0_2, B^0_4, B^3_4, λ, ρ, and H_m, are the model parameters which are usually determined by fitting the experimental energies obtained from infrared or Raman spectra; B^0_2, B^0_4, and B^3_4 are the crystal-field parameters, λ is the spin-orbit coupling, ρ is the spin-spin interaction, H_m is the molecular field acting on the total spin of the atom as a consequence of the magnetic order, g is the gyromagnetic factor of the electron, and μ_B is the Bohr magneton.

(II) Applying the Hund's rules to the free Fe^{2+} ion (with the $3d^6$ electronic configuration in the last shell), we obtain the ground state, which minimizes the electron-electron interactions constrained by the Pauli principle. This ground state of the free Fe^{2+} ion has total orbital and spin quantum numbers, $L = 2$ and $S = 2$, which correspond to a ^5D term consisting of $(2L+1)(2S+1) = 25$ degenerate states. The 25-fold degeneracy is lifted when the free ion is placed inside a solid. For example, the $(2L+1) = 5$ orbital degeneracy is lifted by the crystal-field (electric) potential of the local environment. The crystal-field potential of an ideal O_4 tetrahedron with Fe^{2+} ion in the center lifts the orbital degeneracy of the ^5D multiplet and splits the orbital energy levels in a triplet ($^5T_2$) and a doublet (^5E), in order of increasing energy [52,53], see Fig. 12(a) (the crystal-field states are labeled by the irreducible representations of the local point group with the Fe^{2+} ion placed at the origin). The order of these energy states is reversed when the Fe^{2+} ion is placed at the center of an ideal O_6 octahedron, see Fig. 12(b) [54]. In $Fe_2Mo_3O_8$, the crystal field of the distorted O_4 (O_6) tetrahedra (octahedra) partially lifts the orbital degeneracy and splits the orbital energy levels into two orbital doublets and one singlet. Spin-orbit coupling and spin-spin perturbation further split (and mix) the 25 degenerate states of the ^5D multiplet into a set of doublets and singlets, as shown in Figs. 12(a) and 12(b). In the magnetically-ordered phase, each ion feels a molecular field, which completely lifts the degeneracy of all 25 states of the ^5D multiplet. The cubic symmetry of the O_4 (O_6) tetrahedron (octahedron) is strongly distorted in $Fe_2Mo_3O_8$, giving rise to the trigonal local symmetry (C_{3v} point group). Because of this local symmetry, only three terms ($\mathbf{O}^0_2$, $\mathbf{O}^0_4$, $\mathbf{O}^3_4$) of the crystal-field operator are allowed (the crystal field expansion is written in the basis of angular momentum operators as described below).

To describe the magnetic ground state of the Fe^{2+} ions inside a solid, one needs to solve Schrödinger's equation $\mathbf{H} = E$ in order to get the energies (E) and the eigenfunctions ( ) of both ground and excited states. Considering the commutation relations between $\mathbf{H}$, $\mathbf{L}$, and $\mathbf{S}$, the eigenfunctions of the operator $\mathbf{H}$ can be written as linear combinations

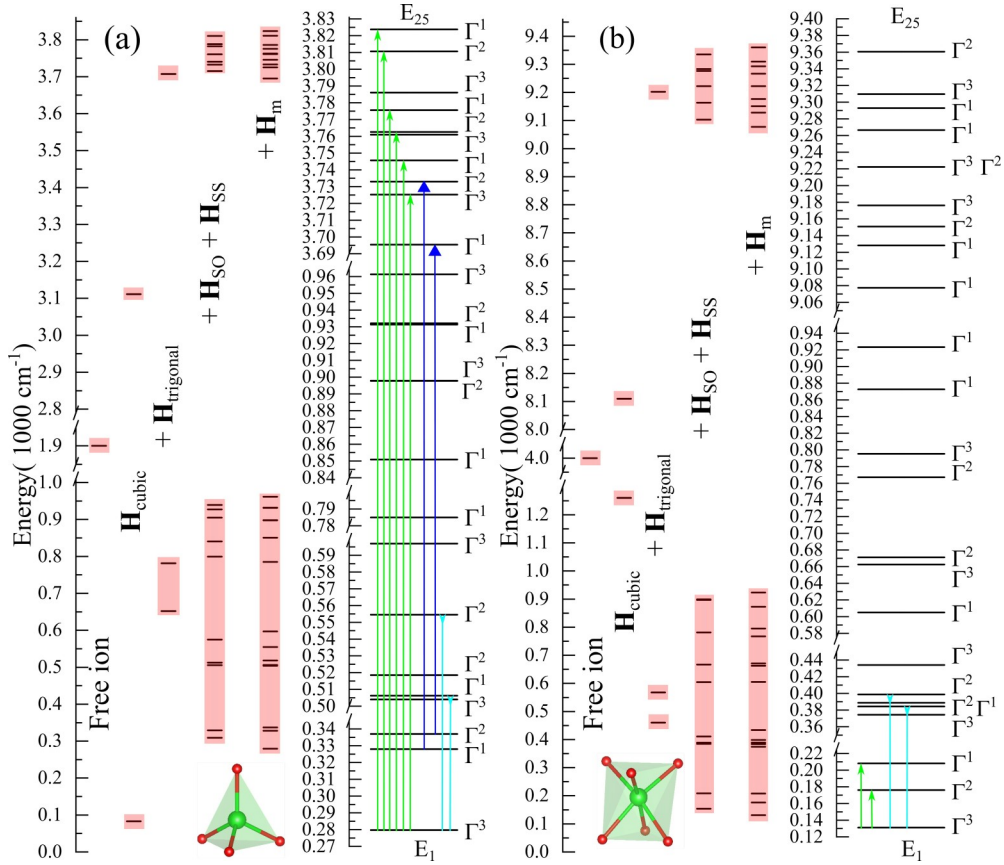

FIG. 12. Energy diagram of the splitting of the ground ^5D term of the Fe $^{2+}$ ($3d^6$) free ion by the (a) tetrahedral and (b) octahedral crystal fields combined with spin-orbit and spin-spin interactions as well as the molecular field due to the magnetic ordering Fe spins below T_N(Fe) = 60 K in $Fe_2Mo_3O_8$. Green lines in (a) correspond to observed infrared and Raman modes in 3400 – 3500 cm^{-1} range. Blue lines in (a) correspond to observed infrared modes attributed to electronic transitions from the first two excited levels of Fe $^{2+}$ (t) ions. Cyan lines in (a) correspond to new modes, which appear in the far-infrared and Raman spectra at $T < T_N$ and can be tentatively attributed to electronic transitions in Fe^{2+} (t) ions by the crystal-field calculations. Green lines in (b) correspond to THz modes observed in Refs. [12,13] which can be related to electronic transitions in Fe $^{2+}$ (o) ions. Blue lines in (b) correspond to new Raman modes observed at $T < T_N$, which can be attributed to electronic transitions in Fe^{2+} (o) ions by the crystal-field calculations.

of the free ion eigenfunctions $|LSM_LM_S\rangle$ classified by the set of quantum numbers L, S, M_L, and M_S, where M_L and M_S are the quantum numbers of the projections of the **L** and **S** operators along a quantization axis. The free ion eigenfunctions can be written as $|LSM_LM_S\rangle = |LM_L\rangle \otimes |SM_S\rangle$, where $\otimes$ is the direct product of the orbital $|LM_L\rangle$ and spin $|SM_S\rangle$ states. Using the Hamiltonian parameters given in Ref. [45], we computed all eigenfunctions Ψ_i ($i \in [1 \cdots 25]$). For each Ψ_i state we have identified the corresponding irreducible representation [55] and used this symmetry information as a constraint in our fits of the Hamiltonian parameters. By symmetry constraints during the fitting procedure, we mean matching the experimental lines in infrared and Raman spectra with those computed electronic transitions, which are allowed by symmetry in the geometry of measurements of experimental lines. We note that due to the molecular field present in the magnetic state, the point group symmetry is artificially lowered from C_{3v} to C_3 (magnetic ordering along the c axis breaks the vertical mirror plane symmetry), thus all the eigenfunctions Ψ_i are labeled by the irreducible representations Γ_i of the C_3 point group. The character tables for C_{3v} and C_3 point groups are reproduced in the Appendix. The energies of the electronic states of Fe^{2+} ions in both oxygen environments (O$_4$ and O$_6$) are given in Table V, together with their irreducible representations. So far we know that IR lines observed in 3400–3500 cm^{-1} range at $T < T_N$ (see Fig. 10 and Table III) are due to electronic transitions of the Fe $^{2+}$ ions inside a tetrahedral oxygen (O$_4$) environment. By fitting these lines, we obtained the Hamiltonian parameters for the tetrahedral site: $B_2^0(t)$, $B_4^0(t)$, $B_4^3(t)$, $\lambda(t)$, $\rho(t)$, and $H_m(t)$. The crystal-field Hamiltonian parameters $B_2^0(o)$, $B_4^0(o)$, $B_4^3(o)$ for the octahedral site were fitted against the low-energy crystal-field level(s) reported in the literature [12,13]. When fitting the octahedral data, the spin-orbit coupling and spin-spin interactions were kept the same as for the tetrahedra, $\lambda(o) = \lambda(t)$, $\rho(o) = \rho(t)$. Due to the scarce availability of the experimental data for the octahedra, more than one solution can be found. Here we report the solution which is in agreement with the magnetization data (the difference between Fe^{2+} magnetic moments for the octahedra and tetrahedra is $\sim 0.5\,\mu_B$) reported in Ref. [8].

Since we know the irreducible representations of each eigenfunction and the irreducible representations for various components of dipole **d** or polarizability $\boldsymbol{\alpha}$ operators, we can predict which transitions are IR or Raman active using

TABLE IV. Wyckoff position, site symmetry, and irreducible representations of atoms for $M_2Mo_3O_8$ (M = Fe, Mn) (space group $P6_3mc$).

Atom	Wyckoff notation	Site symmetry	Irreducible representations
M1	2b	C_{3v}	$A_1 + B_1 + E_1 + E_2$
M2	2b	C_{3v}	$A_1 + B_1 + E_1 + E_2$
Mo	6c	C_s	$2A_1 + A_2 + 2B_1 + B_2 + 3E_1 + 3E_2$
O1	2a	C_{3v}	$A_1 + B_1 + E_1 + E_2$
O2	2b	C_{3v}	$A_1 + B_1 + E_1 + E_2$
O3	6c	C_s	$2A_1 + A_2 + 2B_1 + B_2 + 3E_1 + 3E_2$
O4	6c	C_s	$2A_1 + A_2 + 2B_1 + B_2 + 3E_1 + 3E_2$

Mode classification

$\Gamma_{\text{acoustic}} = A_1 + E_1$

$\Gamma_{\text{Raman}} = 9A_1(xx, yy, zz) + 12E_1(xz, yz) + 13E_2(xy, xx - yy)$

$\Gamma_{\text{IR}} = 9A_1(z) + 12E_1(x, y)$

$\Gamma_{\text{silent}} = 3A_2 + 10B_1 + 3B_2$

symmetry considerations. For the C_3 point group, the components of dipole and polarizability operators transform according to either $_1$ or $_2 + _3$ representations (see Table VIII in the Appendix). If the direct product of representations corresponding to the complex conjugate final states ($^*_1$, $^*_2$, or $^*_3$), the dipole/polarizability operator ($_1$ or $_2 + _3$), and the initial state ($_1$, $_2$ or $_3$) contains the totally symmetric representation $_1$, the transition is allowed, otherwise it is forbidden. For example, consider electric dipole transitions observable in the IR spectra at 5 K. These transitions originate from the ground state $_3$ as it is the only state which is appreciably populated at $T = 5$ K = 3·5 cm^{-1} (see positions of first excited energy levels in Table V, which are above 45 cm^{-1}). The z (x, y) component of the electric dipole operator transforms as $_1$ ($_2 + _3$). A direct product of representations corresponding to transitions due to z component of electric dipole operator, i.e., when an electric field of light e is parallel to the c axis, is

$$_{\text{excited}}{}^* \otimes _1 \otimes _3 = _{\text{excited}}{}^* \otimes _3, \quad (1)$$

and due to x, y components of electric dipole operator, i.e., when $e \perp c$ is

$$_{\text{excited}}{}^* \otimes (_2 + _3) \otimes _3 = _{\text{excited}}{}^* \otimes _1 + _{\text{excited}}{}^* \otimes _2, \quad (2)$$

where $_{\text{excited}}{}^*$ is the complex conjugate representation of the excited state. If $_{\text{excited}} = _1$, then for $e \| c$ geometry [see Eq. (1)], the direct product is $_{\text{excited}}{}^* \otimes _3 = _1 \otimes _3 = _3$, which does not contain the totally symmetric representation $_1$. Thus, an electric dipole transition from the $_3$ ground state to the $_1$ excited state is forbidden when $e \| c$, based on symmetry arguments. On the other hand, for $e \perp c$ geometry [Eq. (2)] the direct product is $^*_1 \otimes _1 + ^*_1 \otimes _2 = _1 + _2$, which contains the fully symmetric representation $_1$. Thus, an electric dipole transition from the $_3$ ground state to the $_1$ excited state is allowed when $e \perp c$. In a similar way, selection rules for electric dipole transitions from any initial state to any final state can be deduced. For the C_3 point group, components of the magnetic dipole operator transform in the same way as components of electric dipole operator, thus if a transition is electric dipole active for $e \| c$ ($e \perp c$), then it is also magnetic dipole active for $h \| c$ ($h \perp c$). To derive selection rules for Raman spectra, we need to consider transformations of polarizability tensor $\boldsymbol{\alpha}$. For example, the direct product of representations corresponding to the Raman transition between the ground state $_3$ and excited state $_3$ activated due to $\boldsymbol{\alpha}_{zz}$ component of polarizability tensor, which transforms as the $_1$ irreducible representation, is $^*_3 \otimes _1 \otimes _3 = ^*_3 \otimes _3 = _2 \otimes _3 = _1$. Since the direct product contains $_1$ representation, the $_3 \rightarrow _3$ transition is allowed in Raman spectra due to $\boldsymbol{\alpha}_{zz}$ component, i.e., in a geometry when electric fields of incident and scattered light are parallel to the c axis. Selection rules for IR and Raman transitions in various geometries for the C_3 point group are summarized in Table IX in the Appendix.

IV. DISCUSSION

A. HT symmetry: Analysis of phonon modes

The combined measurements of single-crystal x-ray diffraction at room temperature and the phonon measurements provide important information about the complex crystal structure of $M_2Mo_3O_8$ (M = Fe, Mn). Our single-crystal x-ray diffraction measurements showed that the crystal structure of these materials at room temperature (also termed as high temperature through this paper) is described by the $P6_3mc$ space group, agreeing with the previously reported data in the literature [6–8].

Using the $P6_3mc$ space group, we have carried out the group-theoretical analysis which predicts 21 IR active phonon modes, $9A_1 + 12E_1$, where A_1 modes are polarized along the c axis ($e \| c$) and E_1 modes—perpendicular to the c axis ($e \perp c$), as shown in Table IV. Our IR data measured at 85 K, i.e., above magnetic ordering temperatures in $M_2Mo_3O_8$ (M = Fe, Mn), reveals 10(9) A_1 and 9(13) E_1 modes for $Fe_2Mo_3O_8$ ($Mn_2Mo_3O_8$), which is in accord with the group theory prediction, thus confirming once again the noncentrosymmetric space group $P6_3mc$ of these materials at high temperatures. Similarly, the group theory predicts 34 Raman active phonon modes, $9A_1 + 12E_1 + 13E_2$, and Raman measurements performed at 85 K reveal 9(10) A_1, 11(12) E_1, and 11(12) E_2 modes for $Fe_2Mo_3O_8$ ($Mn_2Mo_3O_8$) in good agreement with the prediction for the space group $P6_3mc$. The group-theoretical analysis gives the number of modes and their types, but does not provide information about their frequencies. To better understand our data, we performed DFT calculations of phonon modes. The computed frequencies are shown in Table II, along with the experimental frequencies. The crystal structure of $M_2Mo_3O_8$ crystals possessing Fe^{2+} ions in both tetrahedral and octahedral coordination and Mo^{2+}_3 trimmers is rather complex, and so are the underlying atomic motions corresponding to phonon modes. To have a better insight into the latter, in Fig. 13 we show, as an example, the atomic displacements corresponding to two A_1 modes observed in the spectra of $Fe_2Mo_3O_8$. The highest frequency A_1 mode at 852 cm^{-1} involves simultaneous deformations of both Fe and Mo octahedra while the most intense Raman A_1 mode at 446 cm^{-1} is solely due to the motion of MoO_6 octahedra.

TABLE V. Crystal-field energies $E(\mathrm{cm}^{-1})$ and irreducible representations Γ_i ($i = 1, 2, 3$) of corresponding wave functions of Fe^{2+} ions in tetrahedral (t) and octahedral (o) environments of C_3 point symmetry group in $Fe_2Mo_3O_8$. In our notation, the crystal-field level with an ordinal index n ($n \in [1 \cdots 25]$) and irreducible representation Γ_i corresponds to Ψ_n^i wave function. Modes which may be related to phonons are marked with Ph. Mode of unknown origin observed in Ref. [12] at 77 cm^{-1} is marked with ?.

	Tetrahedral site					Octahedral site					
n	$E_{\mathrm{calc}}^{\mathrm{Varret}}$ [45]	Γ_i	$E_{\mathrm{calc}}^{\mathrm{tetra}}$	Γ_i	E_{expt}	$E_{\mathrm{calc}}^{\mathrm{Varret}}$ [45]	Γ_i	$E_{\mathrm{calc}}^{\mathrm{extrap}}$	Γ_i	$E_{\mathrm{calc}}^{\mathrm{octa}}$	Γ_i	E_{expt}
25	4371.2	Γ_1	3544.1	Γ_1	3547	11228	Γ_2	11 340	Γ_2	9229.4	Γ_2	
24	4362.1	Γ_2	3531.0	Γ_2	3529	11210	Γ_3	11 295	Γ_1	9178.6	Γ_3	
23	4355.8	Γ_3	3506.4	Γ_3		11200	Γ_1	11 272	Γ_3	9161.7	Γ_1	
22	4354.6	Γ_1	3495.9	Γ_1	3494	11190	Γ_1	11 261	Γ_1	9135.3	Γ_1	
21	4346.2	Γ_2	3482.9	Γ_2	3481	11170	Γ_2	11 250	Γ_3	9091.2	Γ_3	
20	4344.5	Γ_3	3481.3	Γ_3		11170	Γ_3	11 250	Γ_2	9091.2	Γ_2	
19	4334.0	Γ_1	3465.9	Γ_1	3467	11151	Γ_3	11 238	Γ_3	9045.0	Γ_3	
18	4333.8	Γ_2	3453.3	Γ_2		11141	Γ_2	11 226	Γ_1	9019.6	Γ_2	
17	4332.5	Γ_3	3445.6	Γ_3	3448	11131	Γ_1	11 204	Γ_2	8997.1	Γ_1	
16	4318.0	Γ_1	3415.7	Γ_1		11112	Γ_1	11 158	Γ_1	8946.3	Γ_1	
15	548.1	Γ_3	681.6	Γ_3		575.8	Γ_3	698.6	Γ_3	792.2	Γ_1	
14	540.8	Γ_2	652.4	Γ_2		566.3	Γ_1	694.7	Γ_1	741.5	Γ_1	748^{Ph}
13	537.6	Γ_1	651.7	Γ_1		565.3	Γ_2	669.6	Γ_2	664.2	Γ_3	
12	522.9	Γ_3	618.2	Γ_3		555.6	Γ_2	647.7	Γ_1	636.0	Γ_2	
11	522.6	Γ_2	618.1	Γ_2		552.3	Γ_3	644.8	Γ_2	539.9	Γ_2	
10	473.6	Γ_1	571.1	Γ_1		544.7	Γ_1	641.7	Γ_3	531.4	Γ_3	
9	447.8	Γ_1	505.3	Γ_1		525.3	Γ_1	612.8	Γ_1	473.9	Γ_1	470^{Ph}
8	242.8	Γ_3	317.2	Γ_3		316.3	Γ_3	396.9	Γ_3	302.9	Γ_3	
7	230.1	Γ_2	274.9	Γ_2	270^{Ph}	302.8	Γ_2	346.9	Γ_2	267.5	Γ_2	270^{Ph}
6	192.4	Γ_2	238.8	Γ_2		227.6	Γ_2	287.7	Γ_2	257.6	Γ_1	
5	187.4	Γ_3	226.6	Γ_1	224^{Ph}	224.1	Γ_3	273.8	Γ_3	253.2	Γ_2	253^{Ph}
4	184.9	Γ_1	224.3	Γ_3		182.5	Γ_1	236.5	Γ_1	243.2	Γ_3	
3	20.5	Γ_1	57.3	Γ_2		58.3	Γ_1	84.5	Γ_1	77.0	Γ_1	$77^{?}$[12]
2	15.4	Γ_2	48.3	Γ_1		17.2	Γ_2	62.1	Γ_2	45.0	Γ_2	45[12,13]
1	0.0	Γ_3	0.0	Γ_3		0.0	Γ_3	0.0	Γ_3	0.0	Γ_3	

As has been shown in Sec. III E, using the percentage error to quantify the agreement between the theory and the experiment, we obtain a reasonable agreement within 6% difference. By calculating the percentage error for the individual IR phonon frequency (5.3% for the Mn and 3.8% for the Fe compound) and for the mean (2.1% for the Mn and 5.2% for the Fe compound), we conclude that the agreement is better for the Mn than for the Fe compound. Indeed, by comparing phonon frequencies in Table II, the frequency assignment seems to be good across the whole spectral range for the Mn compound, whereas the calculated low energy phonon frequencies are shifted to higher energies compared to the experimental data for the Fe compound. The reason for this discrepancy could be due to the fact that the ground state electronic structure is not properly accounted within nonspin polarized DFT. Since eDMFT correctly describes the insulating ground state and reproduces well the experimental structural properties, it would be interesting to compute the phonon modes at the eDMFT level [56].

TABLE VI. Parameters $P_{\mathrm{calc}}^{\mathrm{tetra}}$ and $P_{\mathrm{calc}}^{\mathrm{octa}}$ (cm^{-1}) of the crystal-field model used in calculations of the electronic $d - d$ transitions in Fe^{2+} ions in tetrahedral and octahedral sites, respectively. Parameters $P_{\mathrm{calc}}^{\mathrm{Varret}}$ (cm^{-1}) are reproduced here from Ref. [45]. Parameters $P_{\mathrm{calc}}^{\mathrm{extrap}}$ (cm^{-1}) have been used in a preliminary model for the octahedral site and utilize values for the spin-orbit coupling λ, the spin-spin interaction ρ, and the molecular field H_m from the model for the tetrahedral site $P_{\mathrm{calc}}^{\mathrm{tetra}}$, and the rest of the parameters from the model $P_{\mathrm{calc}}^{\mathrm{Varret}}$.

	Tetrahedral site		Octahedral site		
P	$P_{\mathrm{calc}}^{\mathrm{Varret}}$ [45]	$P_{\mathrm{calc}}^{\mathrm{tetra}}$	$P_{\mathrm{calc}}^{\mathrm{Varret}}$ [45]	$P_{\mathrm{calc}}^{\mathrm{extrap}}$	$P_{\mathrm{calc}}^{\mathrm{octa}}$
Dq	400.0	302.8	–1000	–1000	–685
A_2	–22.6	–33.3	–396.0	–396.0	–596.0
A_4	–528.9	–399.4	–170.0	–170.0	–332.0
λ	–100.0	–116.5	–100.0	–116.5	–116.5
ρ	1.0	1.1	1.0	1.1	1.1
H_m	5.0	18.2	5.0	18.2	13.6

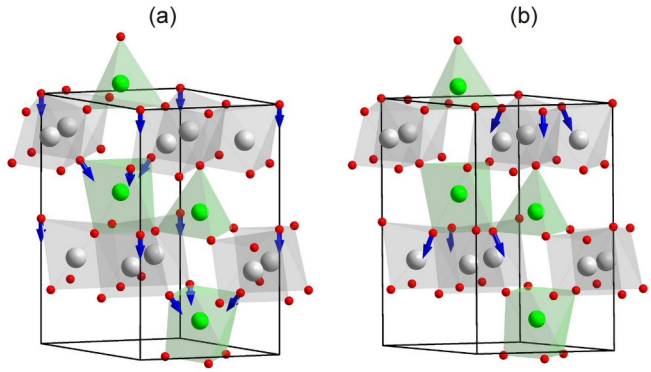

FIG. 13. Atomic displacements corresponding to (a) the highest-frequency A_1 mode at 852 cm^{-1} and (b) the highest-intensity Raman A_1 mode at 446 cm^{-1} in $Fe_2Mo_3O_8$ obtained from the DFT calculations. FeO_4 tetrahedra and FeO_6 octahedra are shown in green and MoO_6 octahedra are shown in gray.

B. HT electronic and structural predictions

Insulating materials with simultaneous magnetic and electric order, called multiferroic materials, usually belong to the class of correlated materials. Modeling the magnetic and electric properties of multiferroic materials is still a challenging problem. For example, the first step in modeling the electric polarization in these materials requires knowledge of two experimental or two theoretical crystal structures; the first one is the high-temperature reference crystal structure where usually polarization is zero and the material is found in the paramagnetic state, and the second one is the low-temperature crystal structure of the multiferroic phase where usually the atomic displacements (that give rise to finite polarization changes) with respect to the reference state are induced by the long-range magnetic order. The chances of finding theoretically the two crystal structures, especially the high-temperature reference structure, has improved due to the recent development of forces for correlated materials in eDMFT [33,57]. While the low-temperature crystal structures can be obtained by spin-polarized DFT, in many cases non-spin-polarized DFT fails to give acceptable results for the high-temperature reference structure, see for example, Table I and Fig. 3. When that happens, one can find an artificial spin-polarized state, which could sometimes give good agreement with the experimental crystal structure even though, in this case, the electronic properties of the experimental paramagnetic state are misrepresented by the artificial spin-polarized state in DFT [58]. The materials studied here are pyroelectrics, which means that the structure possesses already built-in electric moment, and any structural changes induced by temperature, pressure, and magnetic order can induce changes in the electric polarization. Thus, attempts to obtain the high-temperature reference crystal structure in pyroelectric materials by using an artificial spin-polarized state in DFT poses a problem since any type of magnetic order has exchange striction, by which we mean movements of the ligand ions in order to maximize the magnetic energy gain. For example, for $Fe_2Mo_3O_8$ it has been shown in Ref. [8] that the obtained distortion pattern depends on the type of the spin-polarized DFT. Thus, it is difficult to obtain accurate fractional atomic coordinates using DFT for the pyroelectric materials.

Here we performed structural relaxations of the fractional atomic coordinates for fixed lattice parameters using DFT and eDMFT at high temperatures. As discussed in Sec. III and shown in Table I and Fig. 3, eDMFT gives much better agreement with the experimental structural data than DFT does. In addition to a better reproduction of structural properties, eDMFT reproduces very well the electronic properties. For example, Figs. 3(e) and 3(f) show that the total density of states computed for the crystal structure with the relaxed fractional atomic coordinates is almost identical with the total density of states computed for the experimental structure. This is not the case for the same calculations using non-spin-polarized DFT, see Figs. 3(c) and 3(d). Thus, based on these calculations, we can conclude that the coupling between the electronic and lattice degrees of freedom is captured much better in eDMFT than in DFT.

Previously published successful results of structural relaxation in a paramagnetic metallic state, in an insulating ordered state [59], together with the current structural relaxations in the paramagnetic insulating state, strengthen further the predictive power of the eDMFT method for the electronic and structural properties at all temperatures in correlated materials.

C. LT structural changes

As we discussed previously, our room-temperature IR and Raman phonon data agree well with the group theory predictions based on the $P6_3mc$ space group, which was determined by the single-crystal x-ray diffraction measurements. To the best of our knowledge, there are no reports about the symmetry at low temperature. From the measurements of the electrical polarization, see Fig. 1(d), we observed an increase in the electrical polarization concomitantly occuring with the magnetic ordering. This increase suggests that there are structural changes at the magnetic transition in both compounds. Since these materials are pyroelectric, which means that the change in electrical polarization can happen without breaking the symmetry, it is not clear whether the structural changes at the magnetic transition are due to (I) an isostructural phase transition (no change of symmetry away from $P6_3mc$) or (II) a genuine structural phase transition (the symmetry is lowered from $P6_3mc$).

As we have shown so far, three new IR-active modes (E_1 modes at 270, 429, and 470 cm^{-1}) and eight new Raman-active modes (A_1 modes at 232 and 852 cm^{-1}, E_1 mode at 748 cm^{-1}, and E_2 modes at 127, 158, 193, 224, and 253 cm^{-1}) appear in the spectra of $Fe_2Mo_3O_8$ below T_N(Fe) = 60 K. Both new A_1 Raman modes are observed in the IR spectra at 85 K and, thus, they are likely high-temperature modes. The other new lines could be either due to new phonons (signaling the presence of a structural phase transition at $T \sim T_N$), or due to $d - d$ electronic transitions in Fe^{2+} ions.

To test the possibility of the electronic origin of the lines, we have used a crystal-field model developed in Ref. [45], which we further tuned to match our spectroscopic data. Table V shows the computed energies and symmetries of Fe^{2+} electronic states in tetrahedral and octahedral coordinations using several sets of Hamiltonian parameters. $E_{\text{calc}}^{\text{Varret}}$ are the energies obtained using the Hamiltonian parameters $P_{\text{calc}}^{\text{Varret}}$

given in Ref. [45] and reproduced in Table VI. $E_{\text{calc}}^{\text{tetra}}$ are obtained by fitting the Hamiltonian parameters $P_{\text{calc}}^{\text{tetra}}$ to the $d-d$ electronic transitions in Fe^{2+} (t) ions in 3400–3500 cm^{-1}. The calculated energies for the Fe^{2+} (t) ions agree well with the experimental values, except for the 3440 cm^{-1} line, which does not have a calculated counterpart. This line is weak and may correspond to a hybrid excitation, such as a vibronic mode, rather than a pure electronic transition.

The experimental data for the Fe^{2+} (o) electronic levels to fit our model against is scarce. Recent THz measurements of $Fe_2Mo_3O_8$ compounds doped with Zn suggest [12,13] that a line observed at 1 ·25-1·4 THz =~ 45 cm^{-1} in compounds with the doping levels >0.25 can be related to electronic transition in Fe^{2+} (o) ions. Zn doping at levels >0.25 also leads to the appearance of another line at 23 THz = 77 cm^{-1} [12], but its origin is not clear yet. Due to the lack of experimental data, we utilized λ and ρ parameters from our fits of tetrahedra levels and used the rest of Hamiltonian parameters from Ref. [45]. The energy levels $E_{\text{calc}}^{\text{extrap}}$ obtained with this set of parameters ($P_{\text{calc}}^{\text{extrap}}$) are shown in Table V. Two calculated energy levels at 62.1 and 84.5 cm^{-1} are in reasonable proximity to the experimental lines at 45 and 77 cm^{-1}, respectively. According to selection rules shown in Table IX of the Appendix, electronic transitions from the ground $_3$ state to the $_2$ level at 62.1 cm^{-1} and to the $_1$ level at 84·5 cm^{-1} should be observed in $h \perp c$ geometry, which was used for observation of 45 and 77 cm^{-1} lines [12,13]. Although further experimental studies are needed to clarify the origin of the 77 cm^{-1} line, the above arguments suggest that it could be related to electronic transition in Fe^{2+} (o) ions. Assuming this is the case, we tuned Hamiltonian parameters to achieve the best agreement with the 45 and 77 cm $^{-1}$ lines. During the fit, we also used an additional constraint that the calculated difference in magnetic moments for tetrahedral and octahedral sites should match the experimentally determined value of $\sim 0{\cdot}5\,\mu_B$, as reported in Ref. [8]. The obtained energies $E_{\text{calc}}^{\text{octa}}$ and symmetries $_i$ ($i = 1, 2, 3$) of the electronic states of Fe^{2+} (o) ions are given in Table V.

The Hamiltonian parameters that we obtained from our fits are given in Table VI. To be consistent with the literature, instead of giving the crystal-field parameters B's, we are giving a different set of parameters (A_2, A_4, Dq) which are related to the B's by the formulas [45]: $B_2^0 = \frac{A_2}{3}$, $B_4^0 = \frac{A_4}{12} + \frac{Dq}{18}$, $B_4^3 = \frac{-20Dq}{9\sqrt{2}}$. For cubic crystal fields without tetrahedral distortion, only two parameters are needed: $\tilde{\mathbf{H}}_{\text{CF}} = \tilde{B}_4^0\mathbf{O}_4^0 + \tilde{B}_4^3\mathbf{O}_4^3$, where $\tilde{B}_4^3 = B_4^3$ and $\tilde{B}_4^0 = \frac{-\sqrt{2}}{40}B_4^3$. We note that the spin-spin Hamiltonian that we used in our modeling [50,60] is different by a sign from the one used in Ref. [45]. Also, the value we obtained for the spin-spin parameter ρ is similar to other reported values for Fe^{2+} ions [59–63].

Comparison of new IR- and Raman-active modes, which appear in the spectra of Fe $_2Mo_3O_8$ below T_N(Fe) = 60 K, with the calculated energy levels $E_{\text{calc}}^{\text{tetra}}$ for tetrahedral and $E_{\text{calc}}^{\text{octa}}$ for octahedral Fe^{2+} ions shows that out of nine new modes only five modes, namely two E_2 modes at 224 and 253 cm^{-1} and three E_1 modes at 270, 470, and 748 cm^{-1}, can match the calculated electronic transitions based on both energy proximity and compliance with the selection rules from Table IX of the Appendix. The other four modes, namely

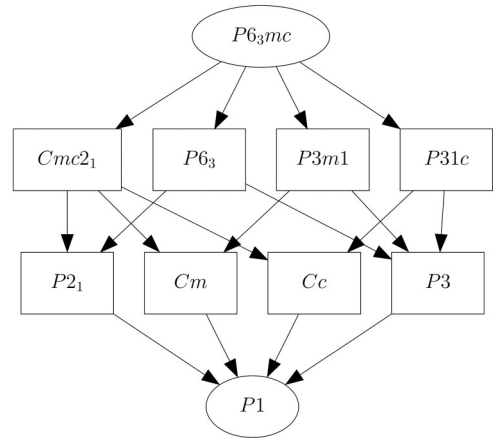

FIG. 14. Group-subgroup diagram. Possible subgroups of the high-temperature parent space group $P6_3mc$ (No. 186) generated by the SUBGROUPGRAPH software for two formula units per unit cell.

E_2 modes at 127, 158, and 193 cm^{-1} as well as E_1 mode at 429 cm^{-1}, are not in the vicinity of any of the calculated energy levels. Besides the obtained set of parameters, which gives the best fit between experiment and theory, we also looked for other solutions that could give a similar agreement. In order to do this, we included each of the four new modes, which cannot be explained as electronic transitions, one by one into the experimental database against which we fit our model, and we were not able to obtain an equally good fit.

Thus, according to our calculations, at least four of the new modes which appear in the spectra of Fe $_2Mo_3O_8$ below T_N(Fe) = 60 K cannot be explained by electronic transitions and should be related to new phonon modes. This indicates the occurrence of structural phase transition concurrent with the magnetic ordering in $Fe_2Mo_3O_8$ compound, which agrees with the conclusion made in Ref. [8]. No spectral changes have been detected for the Mn $_2Mo_3O_8$ compound down to 5 K, suggesting that there is no symmetry change at the magnetic ordering. The existence of the structural phase transition in the Fe compound could be related to the more complex ground state compared to the one in the Mn compound, or to the presence of spin-orbit coupling, which is manifested by the strong Ising-like anisotropy on the magnetic susceptibility data [15].

D. LT symmetry: Possible space groups

As previously shown, our data for $Fe_2Mo_3O_8$ is consistent with a structural transition below T_N. To find out the possible space groups that can describe the crystal symmetry below T_N, we are using the group-subgroup relations. To generate all the possible subgroups for the paramagnetic space group $P6_3mc$ we used the software SUBGROUPGRAPH [64]. Since powder diffraction could not detect any supercell peaks below T_N [65], we generated our group-subgroup diagram with the constraint that the number of formula units per primitive unit cell does not change across the transition. The group-subgroup diagram generated by the software SUBGROUPGRAPH is shown in Fig. 14. As we can see from this diagram, the low symmetry of the crystal could be described by one of the nine possible subgroups.

To limit the number of possibilities for the low-temperature symmetry we turn our attention to the analysis of the IR and Raman modes, in particular to the Raman tensors generated with the software SAM [66] and to the configurations of the backscattering geometry used to probe the Raman spectra. Above T_N the crystal symmetry is described by the space group $P6_3mc$ (No. 186) which has 21 IR active modes $(9A_1 + 12E_1)$ and 34 Raman active modes $(9A_1 + 12E_1 + 13E_2)$. We note that A_1 and E_1 are both Raman and IR active, whereas E_2 modes are only Raman active. This is consistent with our Raman and IR data measured at 85 K, see Table II and Figs. 5(a), 5(b), 6(a), and 7(a)–7(c). Below T_N, our data shows the same trend. The modes observed in the $z(x, y)\bar{z}$ Raman spectra at $T < T_N$, which correspond to E_2 modes at $T > T_N$, do not appear in the IR spectra measured for $e||c$ and $e \perp c$ configurations at $T < T_N$, see Table II and Figs. 5(a), 5(b), and 7(a)–7(c). This implies that the low-temperature space group should have Raman modes that are not IR active. Out of the nine subgroups shown in Fig. 14, only two subgroups satisfy this condition, namely space group $P6_3$ (No. 173) and $Cmc2_1$ (No. 36). Space group $P6_3$ (No. 173) has 36 IR active modes $(12A + 12^1E_1 + 12^2E_1)$ and 62 Raman active modes $(12A + 13^2E_2 + 12^1E_1 + 13^1E_2 + 12^2E_1)$, while space group $Cmc2_1$ (No. 36) has 71 IR active modes $(25A_1 + 21B_1 + 25B_2)$ and 93 Raman active modes $(25A_1 + 22A_2 + 21B_1 + 25B_2)$. Out of the two groups, the $P6_3$ group is the most parsimonious one which can explain our IR and Raman data below T_N. Besides, no supercell peaks were observed in powder diffraction measurements [65] which would otherwise be expected in the case of the $Cmc2_1$ group. Lowering the symmetry from $P6_3mc$ (No. 186) to $P6_3$ (No. 173) removes the degeneracy of E_1 and E_2 modes by splitting them into $^1E_1$ and $^2E_1$, and $^1E_2$ and $^2E_2$ modes, respectively. This is consistent with our data, see Fig. 7(c), where the number of E_2 modes observed in $z(x, y)\bar{z}$ Raman spectra below 300 cm^{-1} nearly doubled across the transition. Besides, the $P6_3$ (No. 173) space group is consistent with the "apparent" C_3 point group symmetry used in modeling the high energy crystal-field levels for the Fe^{2+} sites.

In conclusion, we suggest that the best candidate for the low-temperature crystal structure could be described by the $P6_3$ (No. 173) space group. Further measurements, such as single-crystal neutron scattering, are necessary to validate our prediction.

V. CONCLUSIONS

Optical properties and lattice dynamics of hexagonal $M_2Mo_3O_8$ (M = Fe, Mn) single crystals have been studied experimentally in a wide temperature range by means of infrared reflectivity and Raman scattering. At 85 K, i.e., above the magnetic ordering temperature for both compounds, the far-IR spectra of Fe (Mn) compound reveal 19 (22) IR-active phonons, 10 (9) of them are polarized along the c axis, and 9 (13) are polarized within the ab plane. Raman measurements revealed 9(10), 11(12), and 11(12) Raman-active phonons in $x(z, z)\bar{x}$, $x(z, y)\bar{x}$, and $z(x, y)\bar{z}$ configurations correspondingly for $Fe_2Mo_3O_8$ ($Mn_2Mo_3O_8$) compound. Group theoretical mode analysis and a complimentary density functional theory lattice dynamics calculations are consistent with the $M_2Mo_3O_8$ structure belonging to the high-temperature $P6_3mc$ space group determined from single-crystal x-ray scattering. All observed vibrational modes are assigned to the specific eigenmodes of the lattice. Electronic and structural properties are well reproduced within the eDMFT method for the paramagnetic insulator. These results, combined with previously published results for other electronic states (such as paramagnetic metal and magnetic insulator), prove the predictive power of the eDMFT method in correlated materials, at finite temperatures, over a large electronic, magnetic, and structural phase space.

At temperatures below $T_N(\mathrm{Fe}) = 60$ K, several additional IR- and Raman-active modes are detected in the experimental spectra of the $Fe_2Mo_3O_8$ compound. Crystal-field calculations show that at least four of the new modes cannot be explained by $d - d$ electronic transitions in Fe^{2+} ions and should correspond to new phonon modes. This observation confirms the occurrence of a structural transition in $Fe_2Mo_3O_8$ crystal concurrently with the magnetic ordering of Fe spins. The analysis of our spectroscopic data combined with group-subgroup theory suggests that the best candidate for the low-temperature crystal structure is $P6_3$ (No. 173) space group. On the other hand, no spectral changes have been detected for $Mn_2Mo_3O_8$ compound down to 5 K, whereas the changes in polarization $P(T)$ are similar for both Mn and Fe compounds as they cross the magnetic phase transition. This suggests that the magnetic ordering occurs simultaneously with the isostructural phase transition in the Mn compound. We have also found eight narrow modes in the IR and Raman spectra in 3400– 3500 cm^{-1} range in $Fe_2Mo_3O_8$ compound at $T = 5$ K, which we attribute to the $d-d$ electronic transitions in Fe^{2+} ions in tetrahedral coordination.

Note added. Recently, we became aware of the article by S. Reschke *et al*. [67] reporting analysis of crystal structure and phonon modes in $Fe_2Mo_3O_8$. The infrared and room-temperature x-ray diffraction data in Ref. [67] is reproducing our corresponding data. In addition to infrared measurements, we report Raman measurements, which give access to the E_2 phonon modes, thus enabling a better description of the excitations. Based on the combined IR and Raman data as well as crystal-field calculations, we show that there are at least four new phonon modes, which appear below $T_N = 60$ K, indicating the occurrence of the structural transition at T_N. This is different from the conclusion reported in Ref. [67].

ACKNOWLEDGMENTS

The Raman scattering, IR reflectivity measurements, and sample growth by T.N.S., A.A.S., Y.W., S.W.C., and V.K. were supported by the US Department of Energy DOE DE-FG02-07ER46382. Work at the National Synchrotron Light Source II at Brookhaven National Laboratory was funded by the Department of Energy (Grant No. DE-AC98-06CH10886). Use of the 22-IR-1 beamline was supported by COMPRES under NSF Cooperative Agreement No. EAR 11-57758 and CDAC (Grant No. DE-FC03-03N00144). The State of Texas via the Texas Center for Superconductivity

TABLE VII. Multiplication table for $_1$, $_2$, and $_3$ irreducible representations of the C_3 point group. The table is symmetric.

	1	2	3
1	1	2	3
2	2	3	1
3	3	1	2

provided support to A.P.L. for theoretical calculations. Near-IR-VIS ellipsometry measurements have been performed at the Center for Functional Nanomaterials, which is a US DOE Office of Science Facility, at Brookhaven National Laboratory under Contract No. DE-SC0012704. The DFT and eDMFT work was supported by the US Department of Energy, Office of Science, Basic Energy Sciences, as a part of the Computational Materials Science Program, funded by the US Department of Energy, Office of Science, Basic Energy Sciences, Materials Sciences and Engineering Division in the case of G.L.P. and by NSF-DMR 1709229 in the case of K.H. The crystal-field modeling by G.L.P. was supported from Contract No. 18PFE/16.10.2018 funded by Ministry of Education and Research, Romania within Program 1 - Development of national research and development system, Subprogram 1.2 - Institutional Performance -RDI excellence funding projects. Access to the x-ray facilities at the Research Complex, the Rutherford Appleton Laboratory is gratefully acknowledged. The authors are thankful to K. H. Ahn, E. Nowadnick, and T. A. Tyson at NJIT, and J. L. Musfeldt and K. Park at U. of Tennessee for useful discussions.

APPENDIX

See Tables VII–XII.

TABLE VIII. Character table for $_1$, $_2$, and $_3$ irreducible representations of the C_3 point group. $_2$ and $_3$ irreducible representations are related through complex conjugation: $_2^* = {}_3$ and $_3^* = {}_2$.

				Activity	
C_3	E	C_3	C_3^2	IR	Raman
$_1$	1	1	1	z, S_z	$\alpha_{xx}+\alpha_{yy}, \alpha_{zz}$
$_2$	1	ω[a]	ω^2	$(x,y),(S_x,S_y)$	$(\alpha_{xx}-\alpha_{yy},\alpha_{xy}),(\alpha_{xz},\alpha_{yz})$
$_3$	1	ω^2	ω		

[a] $\omega = e^{2i\pi/3}$.

TABLE IX. Selection rules for electric and magnetic dipole transitions as well as for Raman transitions in backscattering geometries utilized in the study, namely $x(z,z)\bar{x}$, $x(z,y)\bar{x}$, and $z(x,y)\bar{z}$, where $x\|a, z\|c$, and $y\perp(x,z)$, for the C_3 point group.

	1	2	3
1	$e\|\|c; h\|\|c$ $x(z,z)\bar{x}$	$e\perp c; h\perp c$ $x(z,y)\bar{x}; z(x,y)\bar{z}$	$e\perp c; h\perp c$ $x(z,y)\bar{x}; z(x,y)\bar{z}$
2	$e\perp c; h\perp c$ $x(z,y)\bar{x}; z(x,y)\bar{z}$	$e\|\|c; h\|\|c$ $x(z,z)\bar{x}$	$e\perp c; h\perp c$ $x(z,y)\bar{x}; z(x,y)\bar{z}$
3	$e\perp c; h\perp c$ $x(z,y)\bar{x}; z(x,y)\bar{z}$	$e\perp c; h\perp c$ $x(z,y)\bar{x}; z(x,y)\bar{z}$	$e\|\|c; h\|\|c$ $x(z,z)\bar{x}$

TABLE X. Character table for $_1$, $_2$, and $_3$ irreducible representations of the C_{3v} point group.

					Activity	
	C_3	E	$2C_3$	$3\sigma_v$	IR	Raman
A_1	$_1$	1	1	1	z	$\alpha_{xx}+\alpha_{yy}, \alpha_{zz}$
A_2	$_2$	1	1	−1	S_z	
E	$_3$	2	−1	0	$(x,y),(S_x,S_y)$	$(\alpha_{xx}-\alpha_{yy},\alpha_{xy}),(\alpha_{xz},\alpha_{yz})$

TABLE XI. Multiplication table for $_1$, $_2$, and $_3$ irreducible representations of the C_{3v} point group. The table is symmetric.

	1	2	3
1	1	2	3
2	2	1	3
3	3	3	$_1 + {}_2 + {}_3$

TABLE XII. Selection rules for electric and magnetic dipole transitions as well as for Raman transitions in backscattering geometries utilized in the study, namely $x(z,z)\bar{x}$, $x(z,y)\bar{x}$, and $z(x,y)\bar{z}$, where $x\|a, z\|c$, and $y\perp(x,z)$, for the C_{3v} point group.

	1	2	3
1	$e\|\|c$ $x(z,z)\bar{x}$	$h\|\|c$	$e\perp c; h\perp c$ $x(z,y)\bar{x}; z(x,y)\bar{z}$
2	$h\|\|c$	$e\|\|c$ $x(z,z)\bar{x}$	$e\perp c; h\perp c$ $x(z,y)\bar{x}; z(x,y)\bar{z}$
3	$e\perp c; h\perp c$ $x(z,y)\bar{x}; z(x,y)\bar{z}$	$e\perp c; h\perp c$ $x(z,y)\bar{x}; z(x,y)\bar{z}$	$e\|\|c; h\|\|c; e\perp c; h\perp c$ $x(z,z)\bar{x}; x(z,y)\bar{x}; z(x,y)\bar{z}$

[1] J. F. Scott, Applications of magnetoelectrics, J. Mater. Chem. **22**, 4567 (2012).
[2] Y. J. Wang, J. F. Li, and D. Viehland, Magnetoelectrics for magnetic sensor applications: Status, challenges and perspectives, Mater. Today **17**, 269 (2014).
[3] E. Y. Tsymbal, A. Gruverman, V. Garcia, M. Bibes, and A. Barthélémy, Ferroelectric and multiferroic tunnel junctions, MRS Bull. **37**, 138 (2012).
[4] F. Matsukura, Y. Tokura, and H. Ohno, Control of magnetism by electric fields, Nat. Nanotechnol. **10**, 209 (2015).
[5] D. Khomskii, Classifying multiferroics: mechanisms and effects, Physics **2**, 20 (2009).
[6] W. H. McCarroll, L. Katz, and R. Ward, Some ternary oxides of tetravalent molybdenum, J. Am. Chem. Soc. **79**, 5410 (1957).
[7] Y. Le Page and P. Strobel, Structure of iron(II) molybdenum(IV) oxide $Fe_2Mo_3O_8$, Acta Crystallogr. Sect. B **38**, 1265 (1982).
[8] Y. Wang, G. L. Pascut, B. Gao, T. A. Tyson, K. Haule, V. Kiryukhin, and S.-W. Cheong, Unveiling hidden ferrimagnetism and giant magnetoelectricity in polar magnet $Fe_2Mo_3O_8$, Sci. Rep. **5**, 12268 (2015).

[9] T. Kurumaji, S. Ishiwata, and Y. Tokura, Doping-Tunable Ferrimagnetic Phase with Large Linear Magnetoelectric Effect in a Polar Magnet $Fe_2Mo_3O_8$, Phys. Rev. X **5**, 031034 (2015).

[10] T. Kurumaji, S. Ishiwata, and Y. Tokura, Diagonal magnetoelectric susceptibility and effect of Fe doping in the polar ferrimagnet $Mn_2Mo_3O_8$, Phys. Rev. B **95**, 045142 (2017).

[11] T. Kurumaji, Y. Takahashi, J. Fujioka, R. Masuda, H. Shishikura, S. Ishiwata, and Y. Tokura, Electromagnon resonance in a collinear spin state of the polar antiferromagnet $Fe_2Mo_3O_8$, Phys. Rev. B **95**, 020405(R) (2017).

[12] T. Kurumaji, Y. Takahashi, J. Fujioka, R. Masuda, H. Shishikura, S. Ishiwata, and Y. Tokura, Optical Magnetoelectric Resonance in a Polar Magnet $(Fe, Zn)_2Mo_3O_8$ with Axion-Type Coupling, Phys. Rev. Lett. **119**, 077206 (2017).

[13] S. Yu, B. Gao, J. W. Kim, S.-W. Cheong, K. Michael, L. Man, J. Madéo, K. M. Dani, and D. Talbayev, High-Temperature Terahertz Optical Diode Effect without Magnetic Order in Polar $FeZnMo_3O_8$, Phys. Rev. Lett. **120**, 037601 (2018).

[14] T. Ideue, T. Kurumaji, S. Ishiwata, and Y. Tokura, Giant thermal Hall effect in multiferroics, Nat. Mater. **16**, 797 (2017).

[15] S. P. McAlister and P. Strobel, Magnetic order in $M_2Mo_3O_8$ single crystals (M = Mn, Fe, Co, Ni), J. Magn. Magn. Mater. **30**, 340 (1983).

[16] S. Nakayama, R. Nakamura, M. Akaki, D. Akahoshi, and H. Kuwahara, Ferromagnetic behavior of $(Fe_{1-y}Zn_y)_2Mo_3O_8$ ($0 < y < 1$) induced by nonmagnetic Zn substitution, J. Phys. Soc. Jpn. **80**, 104706 (2011).

[17] B. Das, M. V. Reddy, S. Tripathy, and B. V. R. Chowdari, A disc-like Mo-metal cluster compound, $Co_2Mo_3O_8$, as a high capacity anode for lithium ion batteries, RSC Adv. **4**, 33883 (2014).

[18] CrysAlisPro, Oxford Diffraction Ltd., Version 1.171.36.21 (release 14-08-2012 CrysAlis171.NET).

[19] V. Petricek, M. Dusek, and L. Palatinus, Crystallographic computing system JANA2006: General features, Z. Kristallogr. **229**, 345 (2014).

[20] R. C. Clark and J. S. Reid, The analytical calculation of absorption in multifaceted crystals, Acta Crystallogr. Sect. A **51**, 887 (1995).

[21] P. J. Becker and P. Coppens, Extinction within the limit of validity of the Darwin transfer equations. I. General formalism for primary and secondary extinction and their applications to spherical crystals, Acta Crystallogr. Sect. A **30**, 129 (1974); Extinction within the limit of validity of the Darwin transfer equations. II. Refinement of extinction in spherical crystals of SrF_2 and LiF, **30**, 148 (1974); Extinction within the limit of validity of the Darwin transfer equations. III. Non-spherical crystals and anisotropy of extinction, **31**, 417 (1975).

[22] K. Momma and F. Izumi, VESTA 3 for three-dimensional visualization of crystal, volumetric and morphology data, J. Appl. Crystallogr. **44**, 1272 (2011).

[23] The Inkscape Team, Inkscape, http://www.inkscape.org/.

[24] D. M. Ceperley and B. J. Alder, Ground-State of the Electron-Gas by a Stochastic Method, Phys. Rev. Lett. **45**, 566 (1980).

[25] J. P. Perdew and A. Zunger, Self-interaction correction to density-functional approximations for many-electron systems, Phys. Rev. B **23**, 5048 (1981).

[26] K. Refson, P. R. Tulip, and S. J. Clark, Variational density functional perturbation theory for dielectrics and lattice dynamics, Phys. Rev. B **73**, 155114 (2006).

[27] H. J. Monkhorst and J. D. Pack, Special points for Brillouin-zone integrations, Phys. Rev. B **13**, 5188 (1976).

[28] P. Blaha, K. Schwarz, G. K. H. Madsen, D. Kvasnicka, J. Luitz, R. Laskowski, F. Tran, and L. D. Marks, in *WIEN2k, An Augmented Plane Wave + Local Orbitals Program for Calculating Crystal Properties*, edited by K. Schwarz (Techn. Universität Wien, Austria, 2018).

[29] K. Haule, C.-H. Yee, and K. Kim, Dynamical mean-field theory within the full-potential methods: Electronic structure of $CeIrIn_5$, $CeCoIn_5$, and $CeRhIn_5$ Phys. Rev. B **81**, 195107 (2010).

[30] K. Haule, Structural predictions for correlated electron materials using the functional dynamical mean field theory approach, J. Phys. Soc. Jpn. **87**, 041005 (2018).

[31] A. Paul and T. Birol, Applications of DFT+ DMFT in materials science, Annu. Rev. Mater. Res. **49**, 31 (2019).

[32] J. P. Perdew, K. Burke, and M. Ernzerhof, Generalized Gradient Approximation Made Simple, Phys. Rev. Lett. **77**, 3865 (1996).

[33] K. Haule and G. L. Pascut, Forces for structural optimizations in correlated materials within a DFT + embedded DMFT functional approach, Phys. Rev. B **94**, 195146 (2016).

[34] K. Haule and T. Birol, Free Energy from Stationary Implementation of the DFT + DMFT Functional, Phys. Rev. Lett. **115**, 256402 (2015).

[35] K. Haule, Quantum Monte Carlo impurity solver for cluster dynamical mean-field theory and electronic structure calculations with adjustable cluster base, Phys. Rev. B **75**, 155113 (2007).

[36] K. Haule, Exact Double Counting in Combining the Dynamical Mean Field Theory and the Density Functional Theory, Phys. Rev. Lett. **115**, 196403 (2015).

[37] M. T. Hutchings, Point-charge calculations of energy levels of magnetic ions in crystalline electric fields, in *Solid State Physics*, edited by F. Seitz and D. Turnbull (Academic, New York, 1964), Vol. 16, p. 227.

[38] C. Gorller-Walrand and K. Binnemans, Rationalization of crystal-field parametrization, in *Handbook on the Physics and Chemistry of Rare Earths* (North Holland, Amsterdam, 1996), Vol. 23, p. 121.

[39] H. Abe, A. Sato, N. Tsujii, T. Furubayashi, and M. Shimoda, Structural refinement of $T_2Mo_3O_8$ (T = Mg, Co, Zn and Mn) and anomalous valence of trinuclear molybdenum clusters in $Mn_2Mo_3O_8$ J. Solid State Chem. **183**, 379 (2010).

[40] D. Bertrand and H. Kerner-Czeskleba, Structure and magnetic study of transition element molybdates Étude structurale et magnétique de molybdates d'éléments de transition, J. Phys. France **36**, 379 (1975).

[41] Y. Kanazawa and A. Sasaki, Structure of kamiokite, Acta Crystallogr. Sect. C **42**, 9 (1986).

[42] A. B. Kuzmenko, Kramers-Kronig constrained variational analysis of optical spectra, Rev. Sci. Instrum. **76**, 083108 (2005).

[43] A. B. Kuzmenko, Guide to Reffit: Software to fit Optical Spectra, https://sites.google.com/site/reffitprogram/home (2015).

[44] R. Loudon, The Raman effect in crystals, Adv. Phys. **13**, 423 (1964).

[45] F. Varret, H. Czeskleba, F. Hartmann-Boutron, and P. Imbert, Étude par effet Mössbauer de l'ion Fe^{2+} en symétrie trigonale dans les composés du type $(Fe, M)_2Mo_3O_8$ (M = Mg, Zn, Mn, Co, Ni) et propriétés magnétiques de $(Fe, Zn)_2Mo_3O_8$, J. Phys. France **33**, 549 (1972).

[46] G. A. Slack, F. S. Ham, and R. M. Chrenko, Optical absorption of tetrahedral Fe^{2+} ($3d^6$) in cubic ZnS, CdTe, and $MgAl_2O_4$, Phys. Rev. **152**, 376 (1966).

[47] A. M. Lesk, *Introduction to Symmetry and Group Theory for Chemists* (Springer, Netherlands, 2004), p. 97.

[48] R. F. Aroca, Basic principles of IR/Raman: Applications in small molecules structural elucidation, in *Structure Elucidation in Organic Chemistry: The Search for the Right Tools*, edited by M.-M. Cid and J. Bravo (Wiley-VCH, Berlin, 2015), p. 145.

[49] P. W. Atkins and R. S. Friedman, *Molecular Quantum Mechanics* (Oxford University Press, Oxford, 1997).

[50] J. T. Vallin, Dynamic Jahn-Teller effect in the orbital ^5E State of Fe^{2+} in CdTe, Phys. Rev. B **2**, 2390 (1970).

[51] D. Colignon, E. Kartheuser, S. Rodriguez, and M. Villeret, Excitation spectrum of Fe^{2+} in a tetrahedral potential: dynamic Jahn-Teller effect, Phys. Rev. B **51**, 4849 (1995).

[52] M. K. Udo, M. Villeret, I. Miotkowski, A. J. Mayur, A. K. Ramdas, and S. Rodriguez, Electronic excitations of substitutional transition-metal ions in II-VI semiconductors: CdTe: Fe^{2+} and CdSe: Fe^{2+}, Phys. Rev. B **46**, 7459 (1992).

[53] J. W. Evans, T. R. Harris, B. Rami Reddy, K. L. Schepler, and P. A. Berry, Optical spectroscopy and modeling of Fe^{2+} ions in zinc selenide, J. Lumin. **188**, 541 (2017).

[54] W. Low and M. Weger, Paramagnetic resonance and optical spectra of divalent iron in cubic fields. I. Theory, Phys. Rev. **118**, 1119 (1960).

[55] C. Testelin, C. Rigaux, A. Mauger, A. Mycielski, and C. Julien, Dynamic Jahn-Teller effect on the far-infrared spectrum of Fe^{2+} in $Cd_{1-x}Fe_xTe$ compounds, Phys. Rev. B **46**, 2183 (1992).

[56] C. P. Koçer, K. Haule, G. Lucian Pascut, and B. Monserrat, Efficient lattice dynamics calculations for correlated materials with DFT+ DMFT, arXiv:2008.06058.

[57] G. L. Pascut and K. Haule, Role of orbital selectivity on crystal structures and electronic states in $BiMnO_3$ and $LaMnO_3$ perovskites, arXiv:2005.12179.

[58] G. L. Pascut, R. Coldea, P. G. Radaelli, A. Bombardi, G. Beutier, I. I. Mazin, M. D. Johannes, and M. Jansen, Direct Observation of Charge Order in Triangular Metallic $AgNiO_2$ by Single-Crystal Resonant X-Ray Scattering, Phys. Rev. Lett. **106**, 157206 (2011).

[59] K. Haule and G. L. Pascut, Mott transition and magnetism in rare earth nickelates and its fingerprint on the x-ray scattering, Sci. Rep. **7**, 10375 (2017).

[60] U. Kaufmann, EPR and optical absorption of Fe^+, Fe^{2+}, Fe^{3+}, and Fe^{4+} on tetragonal sites in $CdSiP_2$, Phys. Rev. B **14**, 1848 (1976).

[61] R. E. Watson and M. Blume, Spin-spin interaction in paramagnetic ions, Phys. Rev. **184**, 606 (1969).

[62] M. H. L. Pryce, Spin-spin interaction within paramagnetic ions, Phys. Rev. **80**, 1107 (1950).

[63] Y.-Y. Zhou and C.-L. Li, Spin-triplet contribution to zero-field splittings for $3d^4$ and $3d^6$ ions at tetragonal sites, Phys. Rev. B **48**, 16489 (1993).

[64] S. Ivantchev, E. Kroumova, G. Madariaga, J. M. Pérez-Mato, and M. I. Aroyo, Subgroupgraph: A computer program for analysis of group-subgroup relations between space groups, J. Appl. Crystallogr. **33**, 1190 (2000).

[65] S. Choi *et al*. (private communication).

[66] E. Kroumova, M. I. Aroyo, J. M. Perez-Mato, A. Kirov, C. Capillas, S. Ivantchev, and H. Wondratschek, Bilbao crystallographic server: Useful databases and tools for phase-transition studies, Phase Trans. **76**, 155 (2003).

[67] S. Reschke, A. A. Tsirlin, N. Khan, L. Prodan, V. Tsurkan, I. Kézsmárki, and J. Deisenhofer, Structure, phonons, and orbital degrees of freedom in $Fe_2Mo_3O_8$, Phys. Rev. B **102**, 094307 (2020).